NeuroResource

Neuron

Functional Electron Microscopy, "Flash and Freeze," of Identified Cortical Synapses in Acute Brain Slices

Graphical Abstract

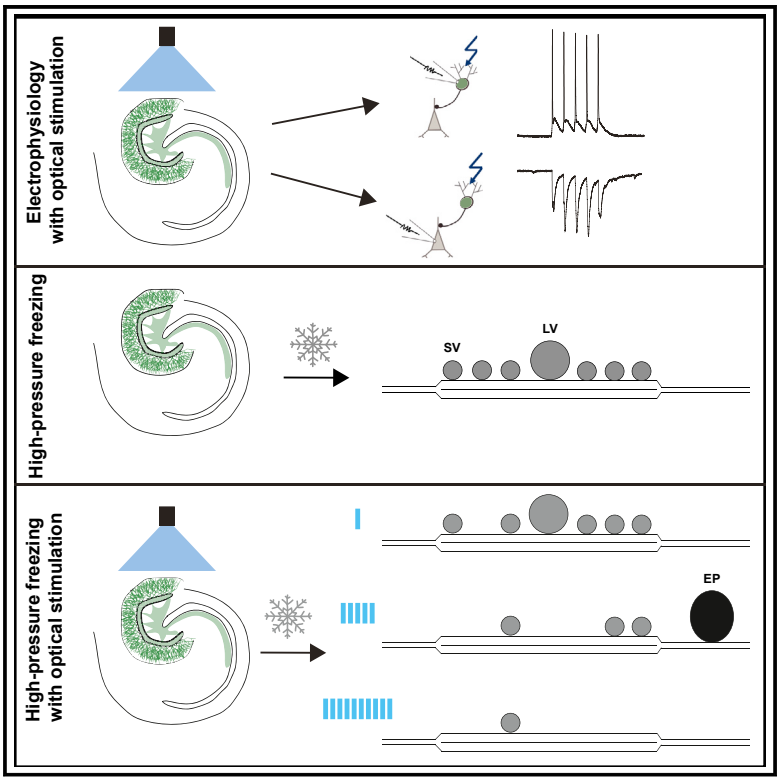

Authors

Carolina Borges-Merjane, Olena Kim, Peter Jonas

Correspondence

carolina.borges-merjane@ist.ac.at (C.B.-M.), peter.jonas@ist.ac.at (P.J.)

In Brief

Borges-Merjane et al. apply functional EM ("flash and freeze") to acute slices and organotypic slice cultures, probing vesicle pool changes at multiple time points during synaptic transmission at an identified cortical synapse, the hippocampal mossy fiber-CA3 pyramidal neuron synapse.

Highlights

- Functional EM may be applied to acute brain slices and organotypic slice cultures
- Docked vesicle pool and RRP are overlapping
- Smaller-diameter vesicles have higher release probability than larger vesicles
- Endocytic pits after moderate stimulation suggest fast endocytosis

Borges-Merjane et al., 2020, Neuron *105*, 992–1006
March 18, 2020
https://doi.org/10.1016/j.neuron.2019.12.022

CellPress

CellPress

Neuron
NeuroResource

Functional Electron Microscopy, "Flash and Freeze," of Identified Cortical Synapses in Acute Brain Slices

Carolina Borges-Merjane,[1,2,*] Olena Kim,[1,2] and Peter Jonas[1,3,*]
[1]Cellular Neuroscience, Institute of Science and Technology Austria, Am Campus 1, 3400 Klosterneuburg, Austria
[2]These authors contributed equally
[3]Lead Contact
*Correspondence: carolina.borges-merjane@ist.ac.at (C.B.-M.), peter.jonas@ist.ac.at (P.J.)
https://doi.org/10.1016/j.neuron.2019.12.022

SUMMARY

How structural and functional properties of synapses relate to each other is a fundamental question in neuroscience. Electrophysiology has elucidated mechanisms of synaptic transmission, and electron microscopy (EM) has provided insight into morphological properties of synapses. Here we describe an enhanced method for functional EM ("flash and freeze"), combining optogenetic stimulation with high-pressure freezing. We demonstrate that the improved method can be applied to intact networks in acute brain slices and organotypic slice cultures from mice. As a proof of concept, we probed vesicle pool changes during synaptic transmission at the hippocampal mossy fiber-CA3 pyramidal neuron synapse. Our findings show overlap of the docked vesicle pool and the functionally defined readily releasable pool and provide evidence of fast endocytosis at this synapse. Functional EM with acute slices and slice cultures has the potential to reveal the structural and functional mechanisms of transmission in intact, genetically perturbed, and disease-affected synapses.

INTRODUCTION

Understanding the relationship between structure and function of synapses is a key issue in neuroscience. Although synaptic structure and function have been studied for decades, several fundamental aspects of synaptic transmission remain unresolved. For example, it is controversial whether synaptic vesicles undergo exocytosis by full fusion or whether the transmitter is released by transient fusion pores (Aravanis et al., 2003; Lisman et al., 2007). Furthermore, the relationship between functionally and structurally defined synaptic vesicle pools remains unclear. Some studies have proposed that the readily releasable pool (RRP) and docked vesicle pool are identical (Schikorski and Stevens, 2001; Imig et al., 2014), whereas others have suggested that the RRP and docked vesicle pool only partially overlap and that vesicles may be released from non-docked pools (Wang et al., 2016). Finally, the mechanisms of endocytosis at central synapses remain elusive. Although it is traditionally thought that vesicles are retrieved from the plasma membrane by clathrin-dependent endocytosis, recent work implicates fast, clathrin-independent mechanisms (Watanabe et al., 2013b; Delvendahl et al., 2016; Chanaday and Kavalali, 2018). Because central synapses are highly diverse, addressing these and other questions requires structural and functional analyses of rigorously identified synapses.

Electron microscopy (EM) is the gold standard for structural analysis of synapses. Almost uniquely, EM provides spatial resolution in the nanometer range. However, a substantial disadvantage of EM is that it only captures static pictures, which typically represent the time point of fixation of the biological preparation. Furthermore, chemical fixation may change the structure of the synapse; for example, by inducing tissue shrinkage or vesicle fusion (Korogod et al., 2015). Alternatively, confocal, two-photon, and optical superresolution imaging may be used to examine synaptic transmission in not only fixed but also living specimens in real time. For example, exocytosis and transmitter release can be studied using synapto-pHluorins, styryl dyes, quantum dots, or transmitter ligand ("sniffer") proteins (Ariel and Ryan, 2010). However, these sophisticated techniques can often only be applied to dissociated cultured neurons, and it is difficult to reach sufficient resolution to identify individual active-zones or single synaptic vesicles. Thus, addressing structure-function relationships at central synapses requires techniques suitable for capturing synapses at both nanometer spatial and millisecond temporal resolutions.

Early attempts to perform concurrent structural and functional analysis of synapses combined electrical stimulation with rapid tissue freezing (Heuser et al., 1979), resulting in structural confirmation of the quantal hypothesis and characterization of synaptic vesicle cycling. Although this approach was successfully applied to the neuromuscular junction, it cannot be readily implemented at central synapses. Recently, some of these limitations were overcome by combining optogenetic stimulation of identified presynaptic neurons with high-pressure freezing (HPF), a technique called "flash and freeze" (Watanabe et al., 2013a). "Flash and freeze" has been successfully applied in the *C. elegans* nervous system (Watanabe et al., 2013a) and in dissociated cultured neurons (Watanabe et al., 2013b). However, for

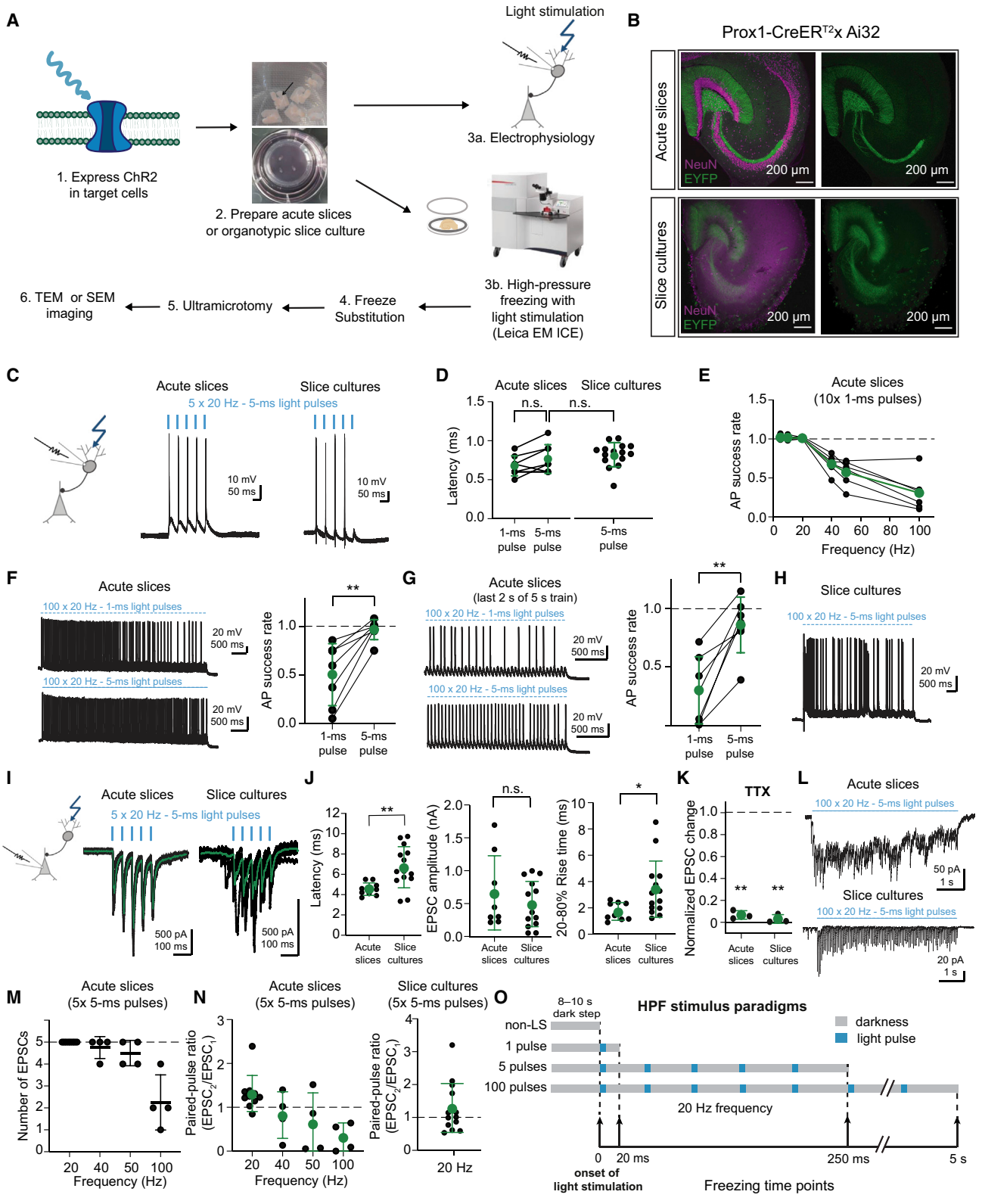

(legend on next page)

intact brain tissue, such as acute slices, selective stimulation of synapses and preservation of the ultrastructure represent severe problems. In particular, it has been widely presumed that HPF techniques cannot be routinely applied to acute slice preparations because the thickness and density of the tissue cause prolonged freezing and formation of ice crystals (Studer et al., 2014). Because our knowledge of the function of synapses is predominantly based on electrophysiological analysis of acute slice preparations (Bischofberger et al., 2006a; Blanton et al., 1989; Edwards et al., 1989; Neher, 2017), the available techniques leave a huge gap between structural and functional data, preventing a unified understanding of synaptic transmission.

Here we describe an improved "flash and freeze" technique to probe structural changes during synaptic transmission at precisely defined time points in identified cortical synapses. Unlike previously reported techniques, the method can be applied to both acute slices and organotypic slice cultures (Figure 1A). This was made possible by the use of thin acute slices, improved carrier geometry, improved recovery protocols, and optimized cryoprotection and freeze substitution. As a proof of principle, we applied the technique to the hippocampal mossy fiber synapse between dentate gyrus granule cells (GCs) and CA3 pyramidal neurons, a key synapse in the hippocampal trisynaptic circuit (Andersen et al., 1971). This synapse has several distinctive structural properties, such as a large presynaptic terminal, a huge number of synaptic vesicles, and variability in vesicle diameter (Chicurel and Harris, 1992; Acsády et al., 1998; Henze et al., 2002; Rollenhagen et al., 2007). Likewise, this synapse has several unique functional characteristics, including low initial release probability and powerful presynaptic plasticity (Salin et al., 1996; Vyleta et al., 2016). How the structural and functional properties relate to each other is unclear. With our improved method, we demonstrate that high-frequency stimulation of GCs depletes the docked vesicle pool at hippocampal mossy fiber synapses, implying that the functionally defined RRP and the structurally defined docked vesicle pool are overlapping (Rizzoli and Betz, 2005; Alabi and Tsien, 2012). Furthermore, we show the appearance of endocytic pit-like structures after moderate stimulation, providing structural evidence of a fast clathrin-independent endocytosis mechanism at this synapse (Delvendahl et al., 2016). Finally, we demonstrate that the technique is widely applicable and can be used in both acute slices and organotypic slice cultures from the mouse hippocampus as well as in acute slices from a variety of brain regions, including the cerebellum and brain stem.

RESULTS

The Prox1 Promoter Selectively Targets Hippocampal GCs

To perform functional EM experiments at identified central synapses in intact neural circuits, we faced several challenges. First, we needed to develop a method to selectively activate the presynaptic neurons; in our case, GCs giving rise to the hippocampal mossy fiber synapses. Prospero homeobox 1 (Prox1) is a transcription factor that determines hippocampal GC identity and is selectively expressed in adult GCs (Lavado et al., 2010; Ming and Song, 2011; Figure 1). To induce Cre expression specifically in GCs, we used a mouse line with constitutive Cre expression, Prox1-Cre, and a line with inducible Cre, Prox1-CreER^{T2} (Bazigou et al., 2011). To quantitatively analyze the proportion of Cre-expressing GCs at the single-cell level, we crossed these Cre lines with a tdTomato reporter line and quantified colocalization with immunoreactivity for NeuN, a pan-neuronal protein (Figures S1A and S1B). In the Prox1-Cre line, 88.3% of GCs expressed tdTomato. In the Prox1-CreER^{T2} line, expression of tdTomato was tamoxifen dose-dependent, approaching the expression in Prox1-Cre mice at high doses (200 mg kg^{-1}; 83.2% in acute slices, 89.3% in slice cultures). We opted to use the Prox1-CreER^{T2} line with timed tamoxifen injections to juvenile mice because labeling was restricted to GCs (Figures S1A and S1B). In contrast, in Prox1-Cre mice, because Cre is functional from birth, we observed developmentally dependent tdTomato labeling of unidentified interneurons (Figure S1C), likely vasoactive intestinal polypeptide-positive interneurons (Miyoshi et al., 2015). To express channelrhodopsin in a large number of GCs, we crossed the Prox1-CreER^{T2} line with an Ai32 (ChR2(H134R)-EYFP) line, injecting high doses of tamoxifen *in vivo* or applying high concentrations of 4-OH-tamoxifen *in vitro* (Figure 1B).

Reliable Optogenetic Activation of GCs and AP-Evoked Synaptic Transmission to CA3 Pyramidal Neurons

Next we determined the optimal settings for optogenetic stimulation (Figures 1C–1O). To achieve this, we performed electrophysiology experiments in acute slices and organotypic slice culture. The intensity of optical pulses was matched to the intensity reached in our HPF apparatus (5.5–8.0 mW mm^{-2}; STAR Methods; Figure 1A). In acute slices, although single 1-ms pulses reliably evoked action potentials (APs) in GCs with minimum latency (Figures 1C and 1D; 1-ms pulses 0.68 ± 0.13 ms

Figure 1. Targeted Labeling and Selective Optogenetic Activation of Hippocampal GCs

(A) Diagram of the "flash and freeze" experimental workflow.

(B) Confocal images of hippocampal acute slices (top) and slice cultures (bottom) of a mouse expressing ChR2-YFP under control of the Prox1 promoter (green), specifically targeting GCs in the dentate gyrus, superimposed with NeuN labeling (magenta). Scale bar size is indicated in the figure.

(C–H) Electrophysiology recordings from GCs in acute slices and slice cultures. Figure shows APs evoked by direct ChR2 activation (in C), measured latency from onset of light pulses of 1 or 5 ms to AP onset (in D), measured optimal frequency of stimulation (in E), and analysis of best frequency in combination with optimal pulse duration resulting in the most optimal AP success rate for both acute slices (in F and G) and slice cultures (in H).

(I–N) Electrophysiology recordings from CA3 pyramidal neurons. Figure shows example EPSCs evoked by synaptic transmission (in I and L), with measured latency from light pulse onset to EPSC onset, EPSC peak amplitude, rise time (in J); application of TTX to block APs evoked in GCs also blocked EPSCs in CA3 pyramidal neurons in acute slices and slice cultures (in K), effect of frequency of stimulation in a brief train of light pulses (in M), and PPR (in N).

(O) Graphic representation of optogenetic stimulus paradigms for HPF experiments, based on assessment of stimulus efficacy by electrophysiology. Light pulses of 5-ms duration applied at maximum 20-Hz frequency were the best parameters determined for EM experiments.

Green circles and whiskers denote mean ± SD. For graphical representation of statistics, *p < 0.05, **p < 0.01, ***p < 0.001, and ****p < 0.0001. See also Figure S1.

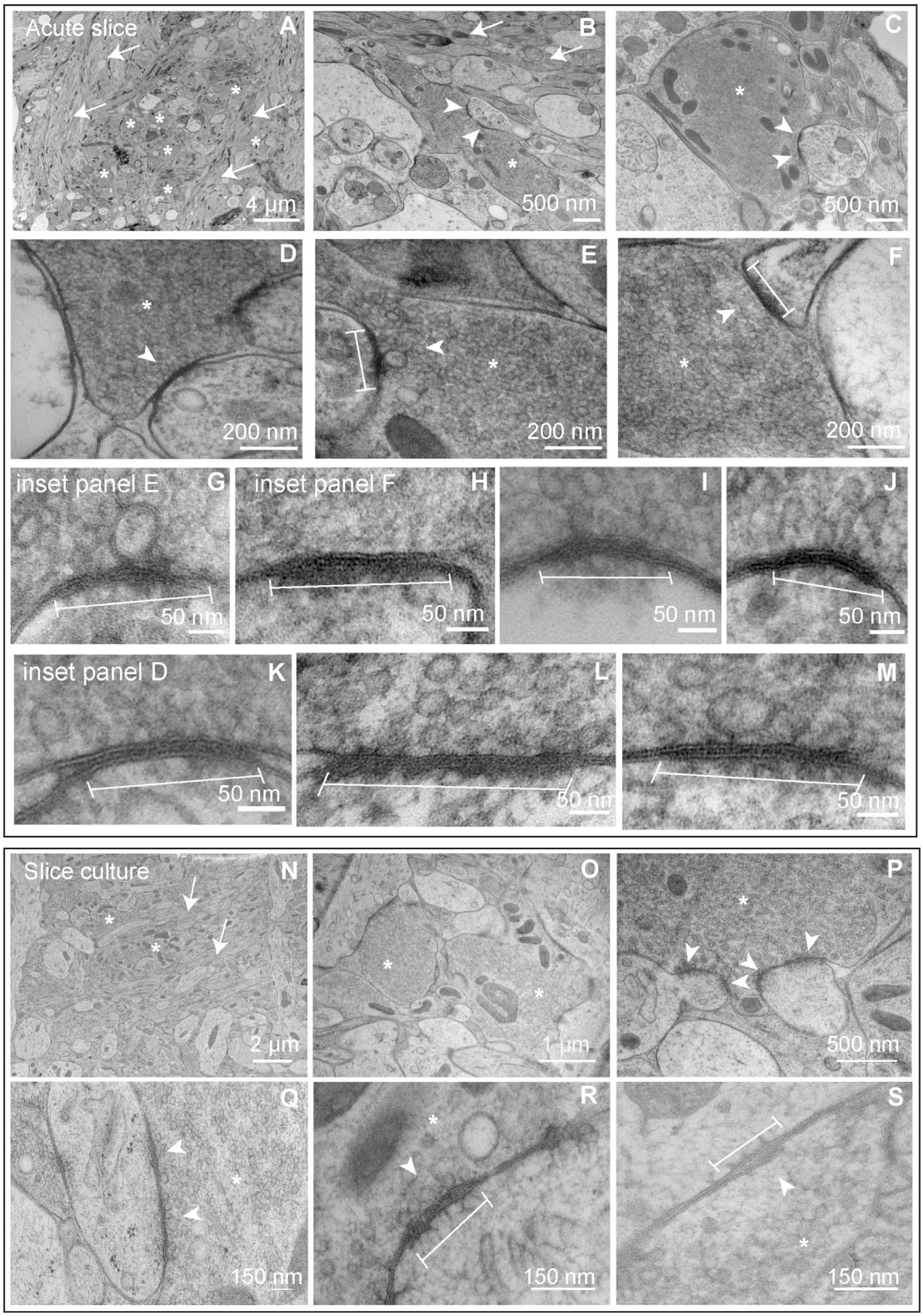

Figure 2. Ultrastructure of High-Pressure-Frozen Acute Slices and Organotypic Slice Cultures

(A–S) Example transmission electron microscopy (TEM) micrographs, showing the quality of the ultrastructure in acute slices (frozen in 15% PVP; A–M) and slice cultures (frozen in 15% BSA; N–S) from lower to higher magnification. Images were taken from the mossy fiber tract in the *stratum lucidum* of the CA3 region,

(legend continued on next page)

[mean ± SD] and 5-ms pulses 0.76 ± 0.18 ms, n = 8 GCs), prolonged trains of 1-ms pulses evoked APs with reduced reliability. This was noticeable in particular over the last 2 s of a 5-s stimulation protocol, with 100 light pulses at a 20-Hz repetition rate, whereas trains of 5-ms pulses reliably evoked APs throughout the stimulus train (Figures 1F and 1G; AP success rate for the entire 5 s stimulation train: 1-ms pulses 0.50 ± 0.32 [mean ± SD], 5-ms pulses 0.96 ± 0.10, p = 0.0034; AP success rate for last 2 s of train: 1-ms pulses 0.30 ± 0.27, 5-ms pulses 0.86 ± 0.22, p = 0.0014; n = 7 GCs). Trains of 10 pulses reliably evoked APs in GCs for stimulation frequencies of up to 20 Hz (Figure 1E). For organotypic slice culture, 1-ms pulses were not sufficient to elicit APs in GCs, whereas 5-ms pulses reliably evoked APs (Figures 1C and 1D; 5-ms pulse latency 0.82 ± 0.16 ms, n = 15 GCs). However, although we observed more failures in slice cultures than in acute slices, we noticed that, with 5-ms pulses, occasionally more than 1 AP was evoked (Figure 1H). Thus, Prox1-CreER^{T2}-driven expression of channelrhodopsin allows reliable optogenetic activation of GCs with single pulses of light and trains of pulses.

Single pulses of light and also 20-Hz trains of 5-ms pulse stimuli led to reliable synaptic transmission to CA3 pyramidal neurons (Figures 1I–1N). Consistent with our observations in GCs, we noted that, above 20-Hz frequency, temporal resolution and fidelity of transmission were lost. For a 5-pulse train, at frequencies greater than 20 Hz, peak amplitudes of excitatory postsynaptic currents (EPSCs) started to overlap, and the paired-pulse ratio (PPR) became variable (Figures 1M and 1N). Interestingly, we observed consistent differences between acute slices and slice cultures. Slice cultures had a longer and more variable latency and slower and more variable rise time, likely because of network rearrangement during the culture growth process (Figure 1J; latency acute slices 4.54 ± 0.62 ms [mean ± SD], n = 9 CA3 pyramidal neurons; slice culture 6.70 ± 2.02 ms, n = 14 CA3 neurons; p = 0.0036; 20%–80% rise time acute slices 1.72 ± 0.62 ms, n = 9 CA3 neurons; slice cultures 3.42 ± 2.14 ms, n = 14 CA3 neurons; p = 0.019). We observed very little recruitment of inhibition with 20-Hz trains of 5-ms pulses. This is presumably due to our experimental configuration, in which the holding potential was close to the chloride equilibrium potential.

Furthermore, bath application of 1 μM tetrodotoxin (TTX) blocked APs in GCs and EPSCs in CA3 pyramidal cells, excluding the possibility that Ca^{2+} inflow through channelrhodopsin channels directly triggered transmitter release (Figure 1K; percent change in EPSC amplitude, 93.2% ± 3.9%; p = 0.0005; n = 3 CA3 pyramidal cells). However, we cannot fully exclude the possibility that Ca^{2+} influx through channelrhodopsin, in combination with presynaptic APs, alters neurotransmitter release. Based on the electrophysiology experiments, single 5-ms pulses and trains of 5-ms pulses of light at 20 Hz were used in subsequent HPF experiments (Figure 1O). Notably, stimulus paradigms such as the long train, with 50 or 100 stimuli at 20 Hz, have been used previously to deplete the RRP (Rosenmund and Stevens, 1996; Murthy and Stevens, 1999).

HPF of Acute Slices for Functional EM Required Several Refinements for Ultrastructure Preservation

To examine central synapses in their native network environment and correlate structural and functional changes during synaptic transmission, we needed to develop a HPF technique for acute slices. Because standard HPF experiments have been demonstrated previously in non-fixed organotypic slice cultures (Studer et al., 2014; Imig et al., 2014), we developed HPF experiments in acute slices and organotypic slice cultures in parallel, using the latter as a reference point for our technical optimization (STAR Methods; Figures 2 and S2–S5).

Several improvements were made to successfully freeze acute slices (Figures 2A–2M, S2, and S3). First, to promote rapid freezing, we decreased the thickness of slices from the standard 250–400 μm used for electrophysiology to 150 and 200 μm (Figures 2A–2M, S2, and S3). Slices of 150-μm thickness had fewer ice crystals in the core of the tissue, whereas 200-μm slices were less fragile and easier to handle. Either could be used for experiments. Second, slices were subjected to a 30- to 45-min recovery period at ~35°C after slicing to improve tissue integrity and recovery of neuronal activity (Bischofberger et al., 2006a), which was important for optogenetic stimulation. Third, we used microcarriers large enough to accommodate the entire slice preparation (6-mm outer diameter) without further trimming (STAR Methods; Figures S2B and S2C). Thus, the entire hippocampal network and part of the surrounding tissue were kept intact. To allow optical stimulation, assembly of the HPF sample sandwich was performed with a pair of transparent sapphire disks (acute slices) or a hybrid sapphire-metal carrier assembly (slice cultures) (Figures S2A and S2B). For slice cultures, the hybrid system resulted in a more stable sandwich configuration because the metal carriers provided a tight fit to hold the membranes of each culture in place (Stoppini et al., 1991). Additionally, transfer of slices to the sapphire sandwich assembly was achieved using a number 4 paintbrush to keep the slice flat, constantly submerged in a drop of artificial cerebrospinal fluid (ACSF), and precisely centered. This is critical to maintain the slice intact as well as to avoid shift of placement, which could lead to sapphire breakage and/or poor freezing quality. Finally, cryoprotectant was added immediately before closing the sandwich assembly. We tested the use of bovine serum albumin (BSA), a commonly used cryoprotectant (Studer et al., 2014), and polyvinylpyrrolidone (PVP) (Möbius et al., 2016). Both are typically used at a 20% concentration. However, to identify the optimum cryoprotectant concentration that would lead to well-preserved ultrastructure without excess exposure, we tested freezing with different concentrations. In organotypic slice cultures, 15% BSA in ACSF resulted in the most well-preserved ultrastructure (STAR Methods). However, in acute slices, 15% PVP in ACSF gave the best result (STAR Methods). One advantage of the

primarily CA3b and CA3c, and show mossy fiber axons (arrows), putative mossy fiber boutons (asterisks), active-zones (arrowheads), and postsynaptic densities (bars). The micrographs in this figure and all supplemental figures associated with Figure 2, are representative of all samples from different mice, used for analysis of controls and light-stimulated tissue, to demonstrate the quality of the ultrastructure across experiments and conditions. Scale bar sizes are indicated in the figure. See also Figures S2–S6.

use of PVP for acute slices is that 15% PVP in ACSF can be equilibrated with carbogen gas (5% CO_2 and 95% O_2), keeping oxygenation and pH constant. To ensure that the addition of PVP did not affect responses to the optical stimulus, we recorded GC APs and optically evoked EPSCs in CA3 pyramidal cells in the presence of 15% PVP. The solution was bath applied by perfusion, and recording began after 1–2 min of equilibration and lasted up to 10 min. This time outlasts exposure to 15% PVP by frozen sections, which was only 1–2 min, at the final stages of sandwich assembly. No significant effects of PVP were observed on latency, EPSC peak amplitude, or PPR (Figure S2D; latency in PVP 5.03 ± 0.50 ms [mean ± SD], p = 0.930; EPSC amplitude in PVP 356.3 ± 18.4 pA; p = 0.6500; PPR in PVP 1.07 ± 0.09; p = 0.3345; n = 3 CA3 neurons). Nonetheless, although we kept the time of exposure to cryoprotectants to the minimum required and performed electrophysiology control experiments, we cannot rule out the possibility that BSA or PVP may have other adverse effects on cellular processes. HPF samples were maintained at physiological temperature (37°C) in the freezing chamber throughout optical stimulation.

Next we tested a variety of freeze substitution protocols based on previous studies that used HPF in fresh (non-fixed) tissue, both organotypic slice cultures and acute slices (Studer et al., 2014), and organotypic slice cultures alone (Imig et al., 2014). We implemented an agitation module that fits on top of the automated freeze substitution system (Goldammer et al., 2016) to shake the samples throughout the procedure. This provided two main benefits. First, by gently shaking the samples, the unopened sapphire sandwiches opened during freeze substitution without damaging the slices, allowing complete infiltration. Second, it notably shortened the duration of the freeze substitution protocol (STAR Methods). After the resulting accelerated procedure, samples underwent room-temperature Durcupan resin infiltration and embedding, followed by ultrathin sectioning and imaging (Figure 1A). Using this procedure, we obtained adequate preservation of the ultrastructure in acute slices, comparable with that of organotypic slice cultures frozen using more conventional procedures (15% BSA; Studer et al., 2014; Figures 2 and S4). Thus, our method is applicable to both acute slices and organotypic slice cultures. Using the same procedure, we also obtained well-preserved ultrastructure in acute 200-μm-thick slices obtained from cerebellum and brain stem (Figure S5). Therefore, our method is generally applicable to acute slices in a variety of brain circuits.

Ultrastructural analysis of HPF material from both acute slices and slice cultures confirmed several previously described properties of hippocampal mossy fiber terminals, including large size, high density of clear synaptic vesicles, presence of large dense-core vesicles, high density of mitochondria, multiple active-zones contacting large spines with dense accumulation of synaptic vesicles in close proximity to the presynaptic membrane, and nonsynaptic *puncta adherentia* contacts with dendritic shafts (Chicurel and Harris, 1992; Henze et al., 2002; Rollenhagen et al., 2007). We focused our ultrastructural analysis on active-zone profiles and peri-active-zone regions (STAR Methods; Figures 2, S2E, and S6). Active-zones were defined as the presynaptic membrane regions directly opposed to the postsynaptic density (asymmetric contacts), with accumulation of clear and round vesicles in close proximity to the membrane and characteristic widening of the synaptic cleft, often showing higher electron density and a disk in the center of the cleft (Chicurel and Harris, 1992; Rollenhagen et al., 2007; Zhao et al., 2012a, 2012b). For ultrastructure analysis, we focused on identifying vesicles docked at identified active-zone areas and also measured their diameters. We confirmed the previously characterized variability in vesicle diameter (Henze et al., 2002; Rollenhagen et al., 2007). We also observed active-zone profiles lacking docked vesicles (Figure S6C). The number of profiles lacking docked vesicles was marginal and not significant under control conditions and increased with stimulation in an activity-dependent manner. Finally, we also identified structures present in the peri-active-zone area within 150 nm of the edge of the active-zone that presumably represent endocytic structures.

The Numbers and Diameters of Docked Vesicles Are Higher in Acute Slices

We first sought to establish a baseline for the number and diameter of docked vesicles in the absence of optical stimulation. To identify any potential effects of the transgenic manipulations from the Prox1-CreER^{T2} x Ai32 mouse line, we compared unstimulated acute slices from wild-type (WT) animals (control) to slices from transgenic animals expressing channelrhodopsin, also without light stimulation (non-LS). Next we compared the non-LS samples from acute slices with non-LS samples from slice cultures to identify potential changes as a consequence of *in vitro* development of the circuit in culture (Figure 3). The number of docked vesicles was expressed as density per 100 nm of active-zone profile.

The numbers and diameters of docked vesicles were not significantly different between WT and non-LS control conditions (Figure 3; in WT: number of docked vesicles 1.25 ± 0.46 [mean ± SD], median 1.23; docked vesicle diameter 38.9 ± 13.4 nm, median 35.1 nm; n = 123 active-zone profiles, n = 366 vesicles, N = 2 mice; in non-LS: number of docked vesicles 1.16 ± 0.49, median 1.14; docked vesicle diameter 37.7 ± 13.4 nm; median 33.8 nm; n = 116 active-zone profiles, n = 280 vesicles, N = 3 mice; WT versus non-LS: number of docked vesicles p = 0.5428; vesicle diameter p = 0.1962). However, the numbers and diameters of docked vesicles were significantly higher in acute slices (Figure 3; in culture non-LS: number of docked vesicles [mean ± SD] 0.84 ± 0.52; median 0.77; docked vesicle diameter 36.7 nm ± 17.8 nm; median 31.5 nm; n = 170 active-zone profiles, n = 171 vesicles, N = 3 mice; non-LS acute slices versus non-LS slice cultures: number of docked vesicles p < 0.0001 and diameter p = 0.0145; Figure 3A, left and right panels, respectively). Furthermore, the docked vesicle diameter distribution was continuous and right-skewed in acute slices, whereas it was more bimodal in organotypic slice cultures (Figures 3D and 3E). Maximum likelihood analysis revealed no significant improvement of the fit with two components in acute slices (p = 0.59) but a better fit in organotypic slice cultures (p < 0.001; STAR Methods). For direct comparison across groups during analysis of the frequency distribution of vesicle diameters, raw histogram counts were divided by the total length of active-zone analyzed for each corresponding experimental condition. The resulting histograms display vesicle density (per 100 nm of active-zone) as a function of vesicle diameter, as shown in Figure 3D.

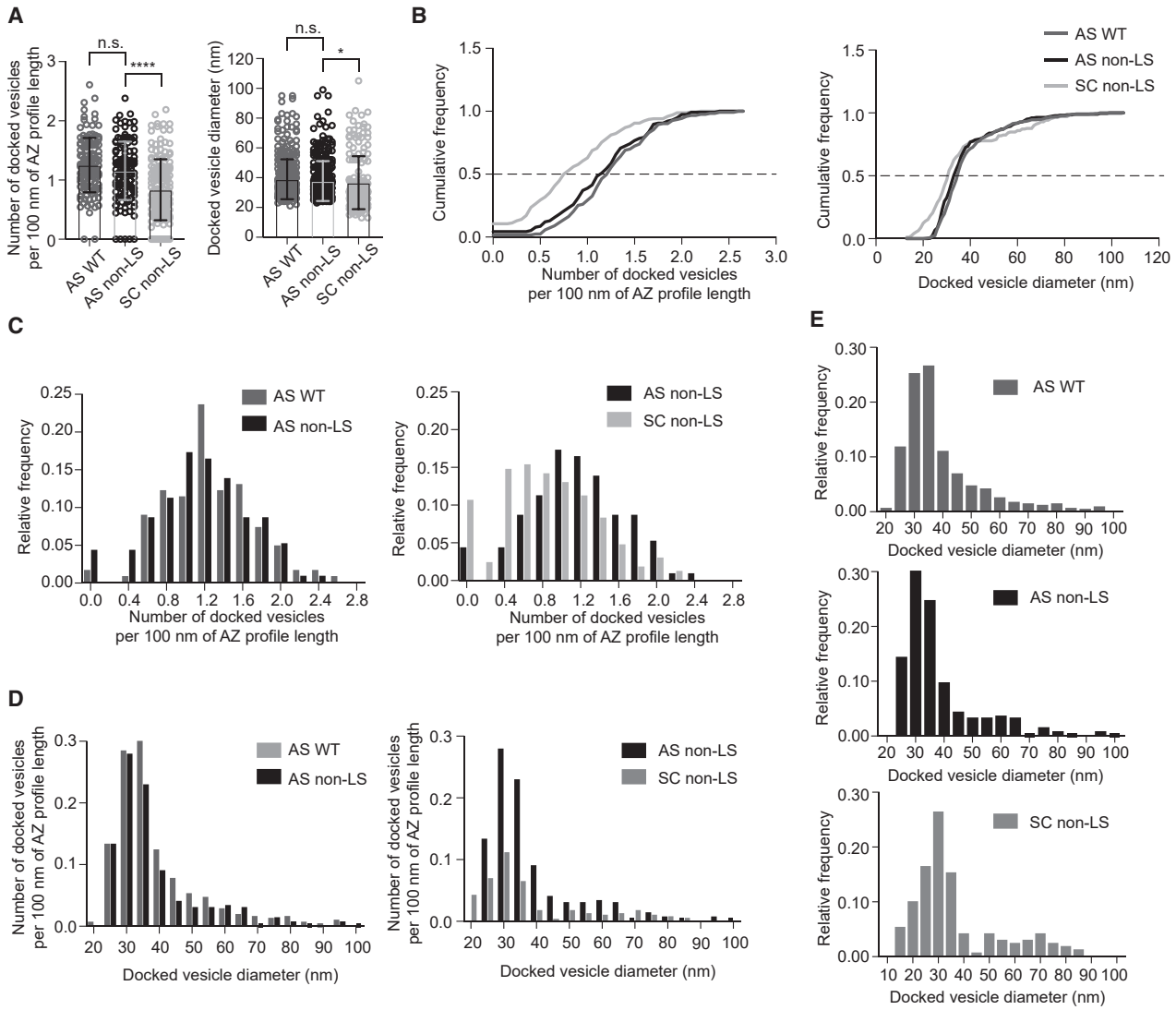

Figure 3. Mossy Fiber Boutons in Acute Slices Have More Docked Vesicles and Larger-Diameter Vesicles Than in Slice Cultures

(A) Left panel: scatterplot of the number of docked vesicles per 100 nm of active-zone length in acute slices (ASs) from wild-type (WT) animals and from non-light-stimulated transgenic animals (non-LS) and slice cultures (SCs) from non-light-stimulated transgenic animals (non-LS). Right panel: scatterplot of the diameter of docked vesicles in each group. Bars and whiskers show mean ± SD. For graphical representation of statistics, *$p < 0.05$, **$p < 0.01$, ***$p < 0.001$, and ****$p < 0.0001$.

(B) Cumulative plots of the data displayed in (A) for the number of docked vesicles (left) and docked vesicle diameter (right).

(C) Histograms with the relative frequency distribution of the number of docked vesicles per 100 nm of active-zone length compared between AS controls (WT versus non-LS) and between ASs and SCs (AS non-LS versus SC non-LS).

(D) Histograms of docked vesicle diameter compared between AS controls (WT versus non-LS) and between ASs and SCs (AS non-LS versus SC non-LS).

(E) Histograms showing the individual relative frequency distribution of docked vesicle diameter for ASs and SCs.

See also Figure S7.

Finally, to test whether any basal AP activity would affect the measurements of the size of the docked pool, we performed a TTX control of non-light-stimulated transgenic animals in the presence of 1 μM TTX (non-LS+TTX) (Figure S7). Neither numbers nor diameters of docked vesicles were significantly different across acute slice control conditions (in non-LS+TTX: number of docked vesicles 1.15 ± 0.57; median 1.07; docked vesicle diameter 39.7 ± 15.1 nm; median 34.4 nm; n = 102 active-zone profiles, n = 252 vesicles, N = 2 mice; WT versus non-LS+TTX: number of docked vesicles p = 0.6465 and vesicle diameter p = 0.8194; non-LS versus non-LS+TTX: number of docked vesicles p > 0.9999 and vesicle diameter p > 0.9999). There was also no significant difference for slice cultures (in non-LS+TTX: number of docked vesicles 0.77 ± 0.48; median 0.69; docked vesicle diameter 40.3 ± 20.1 nm; median 32.8 nm; n = 154 active-zone profiles, n = 124 vesicles, N = 2

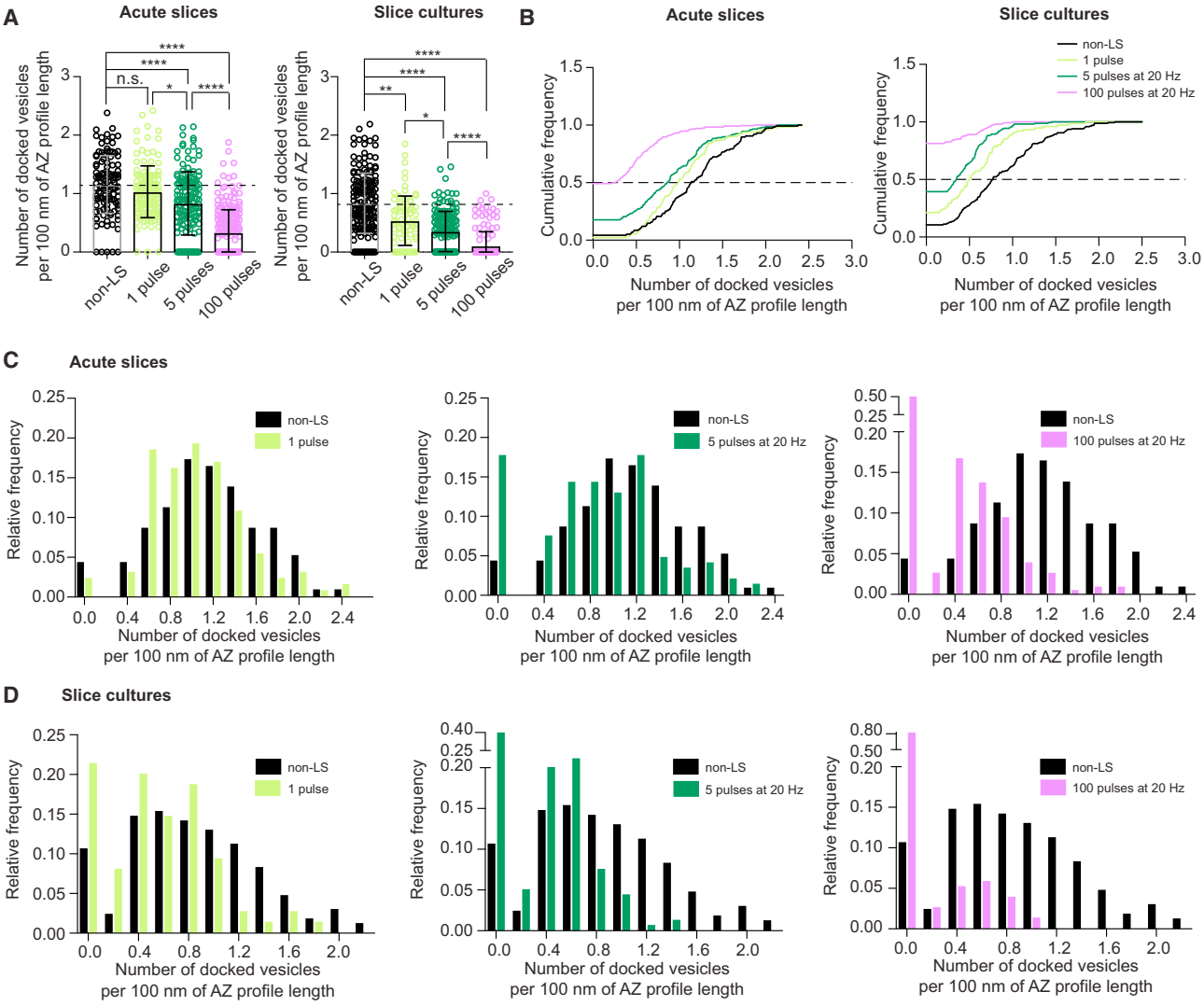

Figure 4. The Number of Docked Vesicles Decreases in an Activity-Dependent Manner in Both ASs and SCs

(A) Scatterplot of the number of docked vesicles per 100 nm of active-zone length in ASs (left) and SCs (right) for each stimulation paradigm. Bars and whiskers show mean ± SD. For graphical representation of statistics, *p < 0.05, **p < 0.01, ***p < 0.001, and ****p < 0.0001. Dashed line indicates the mean of non-LS control.

(B) Cumulative plots of the data displayed in (A). Dashed line indicates the median.

(C and D) Histograms showing the comparison of relative frequency distribution of docked vesicle numbers for ASs (C) and SCs (D). The histograms compare each stimulated sample with non-LS control.

mice; non-LS versus non-LS+TTX: number of docked vesicles p > 0.9999 and vesicle diameter p > 0.9999).

Taken together, these results indicate that the numbers and diameters of docked vesicles in slices from transgenic mice are similar to the WT and unaffected by basal AP activity. However, the numbers and diameters are slightly but significantly higher in acute slices than in organotypic slice cultures.

Stimulus-Dependent Depletion of the Docked Vesicle Pool

Finally, we analyzed the effect of mild and strong optical stimulation on the numbers and diameters of docked vesicles in active-zone profiles of mossy fiber boutons in acute slices and organotypic slice cultures (Figures 4 and 5). For this purpose, we applied three paradigms widely used in electrophysiology experiments (Figure 1O): 1 pulse of light that evoked 1 AP in acute slices or 1–2 APs in the case of slice cultures; a brief train of 5 pulses at 20 Hz; and a long train of 100 pulses at 20 Hz, a stimulus commonly used to deplete the RRP (Rosenmund and Stevens, 1996; Murthy and Stevens, 1999). Based on the time course of exocytosis measured previously with similar approaches (Watanabe et al., 2013a, 2013b), after a single optical pulse, samples were frozen 20 ms after pulse onset in an attempt to capture vesicle fusion evoked by a single AP. For the brief and long trains of pulses delivered at 20 Hz, samples were frozen 50 ms after last pulse onset (Figure 1O). We examined structural correlates of both exocytosis

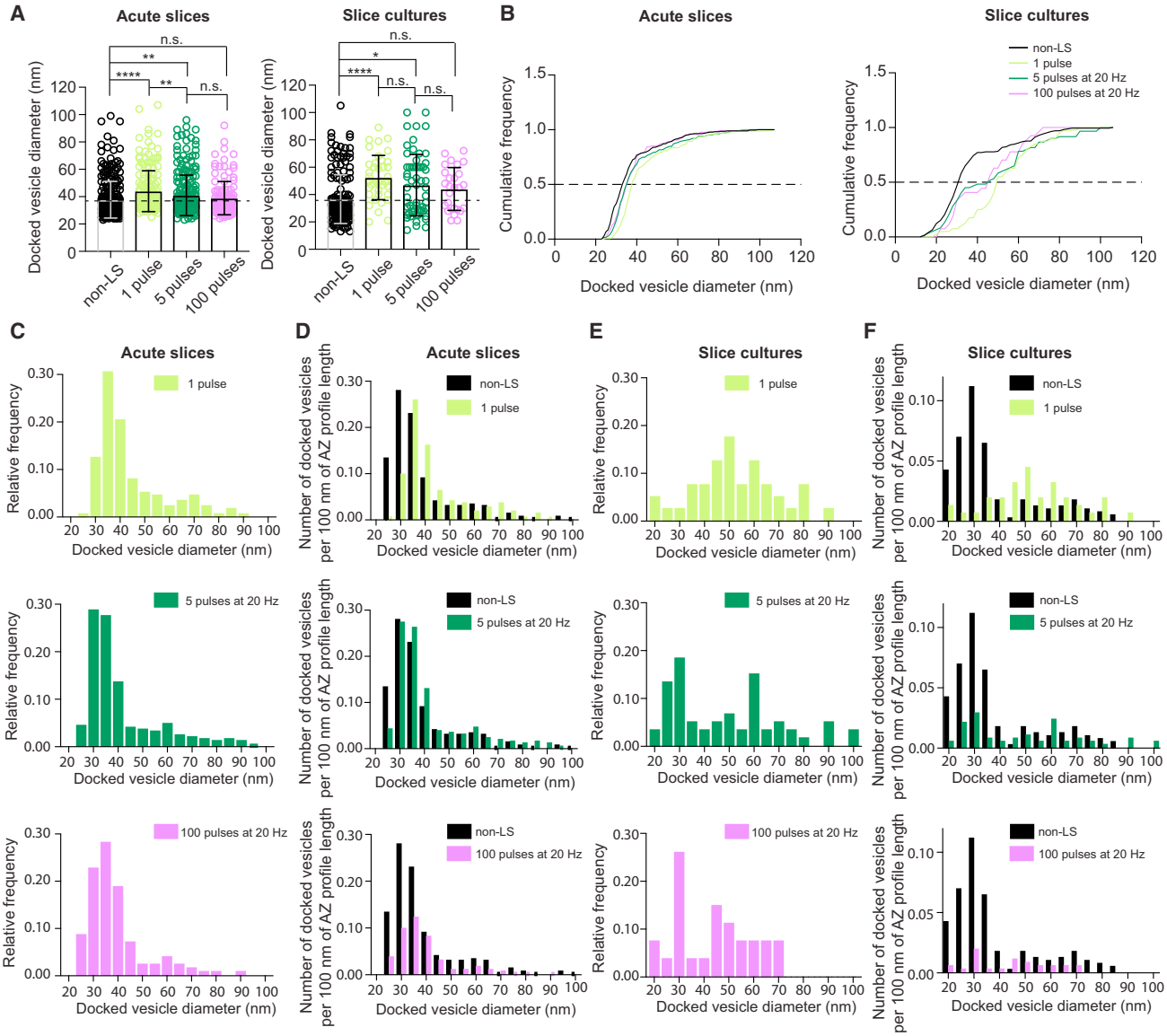

Figure 5. The Mean Diameter of Docked Vesicles Changes in an Activity-Dependent Manner in ASs and SCs

(A) Scatterplot of the diameter of docked vesicles measured in ASs (left) and SCs (right) for each stimulation paradigm. Bars and whiskers show mean ± SD. For graphical representation of statistics, *$p < 0.05$, **$p < 0.01$, ***$p < 0.001$, and ****$p < 0.0001$. Dashed line indicates the mean of non-LS control.

(B) Cumulative plots of the data displayed in (A). Dashed line indicates the median.

(C) Histograms showing the relative frequency distribution of docked vesicle diameter for stimulated groups in ASs.

(D) Comparison of docked vesicle diameter between non-LS control and stimulated groups in ASs.

(E) Histograms showing the relative frequency distributions of docked vesicle diameter for stimulated groups in SCs.

(F) Comparison of docked vesicle diameter between non-LS control and stimulated groups in SCs.

and endocytosis. As above, the number of docked vesicles was quantified as density per 100 nm of active-zone profile.

In samples exposed to a single pulse, we observed a decrease in the mean number of docked vesicles in comparison with non-LS control conditions, albeit only significant in slice cultures (acute slices, Figures 4A–4C; mean ± SD 1.03 ± 0.44; median 0.99; n = 130 active-zone profiles, N = 2 mice; p = 0.7015; Figure 4A, left panel; slice cultures: Figures 4A, 4B, and 4D; 0.54 ± 0.42; median 0.51; n = 75 active-zone profiles, N = 3 mice; p = 0.0017; Figure 4A, right panel). This could be due to our observation that, on occasion, a single pulse evoked more than 1 AP in slice cultures. Furthermore, we observed a significant increase in the mean diameter of docked vesicles (acute slices: Figures 5A–5D; mean ± SD 44.0 ± 15.0 nm; median 38.2 nm; n = 130 active-zone profiles, n = 177 vesicles, N = 2 mice; p < 0.0001; Figure 5A, left panel; slice cultures: Figures 5A, 5B, 5E, and 5F; mean ± SD 52.5 ± 16.2 nm; median 50.1 nm; n = 75 active-zone profiles, n = 40 vesicles, N = 3 mice; p < 0.0001; Figure 5A, right panel). These results suggest that, following a single

pulse of light, docked vesicles with smaller diameter were preferentially released.

In samples exposed to 5 pulses of light at 20 Hz, we observed a further significant decrease in the number of docked vesicles as compared with non-LS control in acute slices (Figures 4A–4C; mean ± SD 0.83 ± 0.54; median 0.86; n = 147 active-zone profiles, N = 3 mice; non-LS control versus 5 pulses $p < 0.0001$ and 1 pulse versus 5 pulses $p = 0.0169$; Figure 4A, left panel) and in slice cultures (Figures 4A, 4B, and 4D; mean ± SD 0.35 ± 0.34; median 0.35; n = 160 active-zone profiles, N = 3 mice; non-LS control versus 5 pulses $p < 0.0001$ and 1 pulse versus 5 pulses $p = 0.0203$; Figure 4A, right panel). Furthermore, the diameter of docked vesicles was significantly increased compared with non-LS control for both acute slices (Figures 5A–5D; mean ± SD 40.9 ± 14.8 nm; median 35.2 nm; n = 147 active-zone profiles, n = 251 vesicles, N = 3 mice; $p = 0.0029$; Figure 5A, left panel) and slice cultures (Figures 5A, 5B, 5E, and 5F; mean ± SD 46.9 ± 22.5 nm; median 45.3 nm; n = 160 active-zone profiles, n = 60 vesicles, N = 3 mice; $p = 0.0124$; Figure 5A, right panel). Although still larger than the non-LS control, the mean and the median diameter of docked vesicles, after a short train, were smaller than after a single pulse of light, albeit this was only significant in data from acute slices ($p = 0.0014$). These results suggest that, following a brief train of pulses, both smaller- and larger-diameter vesicles were released. Additionally, with this stimulus paradigm, we observed significantly more putative endocytic structures in the peri-active-zone area, within 150 nm from the active-zone edge, than under any other condition (Figure 6; acute slices non-LS control versus 1 pulse $p > 0.9999$, non-LS control versus 5 pulses $p < 0.0001$, non-LS control versus 100 pulses $p > 0.9999$ and slice cultures non-LS control versus 1 pulse $p > 0.9999$, non-LS control versus 5 pulses $p < 0.0001$, non-LS control versus 100 pulses $p > 0.9999$). Similar experimental approaches using "flash and freeze" in dissociated neuronal cultures (Watanabe et al., 2013b) revealed endocytic structures appearing between 100–300 ms after an optical pulse stimulus and cleaving off up to 1 s thereafter. Furthermore, capacitance measurements from hippocampal mossy fiber terminals suggested fast endocytosis with a time constant of 470 ms at near-physiological temperature (Hallermann et al., 2003; Delvendahl et al., 2016). The short stimulus train of 5 pulses at 20 Hz, used in the present experiments, lasted 250 ms from onset of the first pulse. Thus, putative endocytic structures may have originated as a consequence of the first 3–4 pulses on the train. The diameter of these putative endocytic structures was, on average, 63.6 ± 3.5 nm, approximately twice the size of a synaptic vesicle, and was not significantly different among any groups (Figure 6B). We also addressed whether the presence of endocytic pits was different between acute slices and slice cultures by further testing statistical significance. We only found a significant difference between the 5-pulse stimulation groups (acute slices versus slice culture non-LS control $p > 0.9999$, 1 pulse $p > 0.9999$, 5 pulse $p < 0.0001$, 100 pulse $p > 0.9999$) (Figure 6C).

In samples exposed to 100 optical pulses at 20 Hz, there was a substantial further decrease in the number of docked vesicles both in acute slices (Figures 4A–4C; mean ± SD 0.33 ± 0.39; median 0.25; n = 234 active-zone profiles, N = 3 mice; $p < 0.0001$; Figure 4A, left panel) and in slice cultures (Figures 4A, 4B, and 4D; mean ± SD 0.11 ± 0.24; median 0.00; n = 155 active-zone profiles, N = 3 mice; $p < 0.0001$; Figure 4A, right panel). This is consistent with the hypothesis that docked vesicles are part of the RRP (Schikorski and Stevens, 2001). However, although we observed a 71.5% decrease in the number of docked vesicles compared with the non-LS control, there were still docked vesicles present. This suggests that either not all docked vesicles are part of the RRP or that the docked vesicle pool undergoes rapid refilling during the 5-s stimulus train. The diameter of docked vesicles after the depleting stimulus was not different from the diameter under non-LS control conditions (acute slices, Figures 5A–5D; mean ± SD 38.9 ± 12.1 nm; median 35.4 nm; n = 234 active-zone profiles, n = 128 vesicles, N = 3 mice; $p > 0.9999$; Figure 5A, left panel; slice cultures: Figures 5A–5C; 44.1 ± 15.7 nm; median 45.1 nm; n = 155 active-zone profiles, n = 27 vesicles, N = 3 mice; $p > 0.9999$; Figure 5A, right panel) and neither from that observed with a short stimulus train. Thus, with an RRP-depleting stimulus, both smaller- and larger-diameter docked vesicles were released.

Is it possible that the large docked vesicles in the active-zones are confused with endocytic pits? Although we cannot completely exclude this, several observations argue against this possibility. First, the diameter of large putative docked vesicles (>40 nm in diameter) in the active-zone is significantly smaller than that of endocytic structures in the peri-active-zone area ($p < 0.0001$). Second, large putative docked vesicles are present under control conditions (Figure 3; Figure S7). Third, activity-dependent changes in large putative docked vesicles are opposite to those observed for endocytic pits. For instance, with the 5 pulses at 20-Hz stimulation, the absolute number of large putative docked vesicles in the active-zone remained unchanged (Figure 5D, center), whereas the number of endocytic pits in the peri-active-zone increased (Figure 6C). Conversely, with the 100 pulses at 20-Hz stimulation, the number of large putative docked vesicles in the active-zone declined (Figure 5D, bottom), whereas the number of endocytic pits in the peri-active-zone returned to control levels. Thus, it is more likely that the large structures within the active-zone region are "giant" synaptic vesicles, identified previously in mossy fiber terminals (Henze et al., 2002; Figures S2E and S6C).

DISCUSSION

In cellular neuroscience, a huge gap exists between structural analysis by EM and functional analysis by electrophysiology and optical imaging. Although EM has exquisitely high spatial resolution (Palay, 1956; Schikorski and Stevens, 1997; Harris and Weinberg, 2012), it only generates static pictures. In contrast, electrophysiology has microsecond temporal resolution but provides limited spatial information. Traditionally, completely different preparations are used for morphological and functional experiments. EM is typically applied in combination with perfusion fixation of whole brains for optimal tissue preservation, whereas electrophysiology is largely performed in acute slices (Bischofberger et al., 2006a; Blanton et al., 1989; Edwards et al., 1989). Thus, correlating structural and functional information is a major challenge. The present paper reports

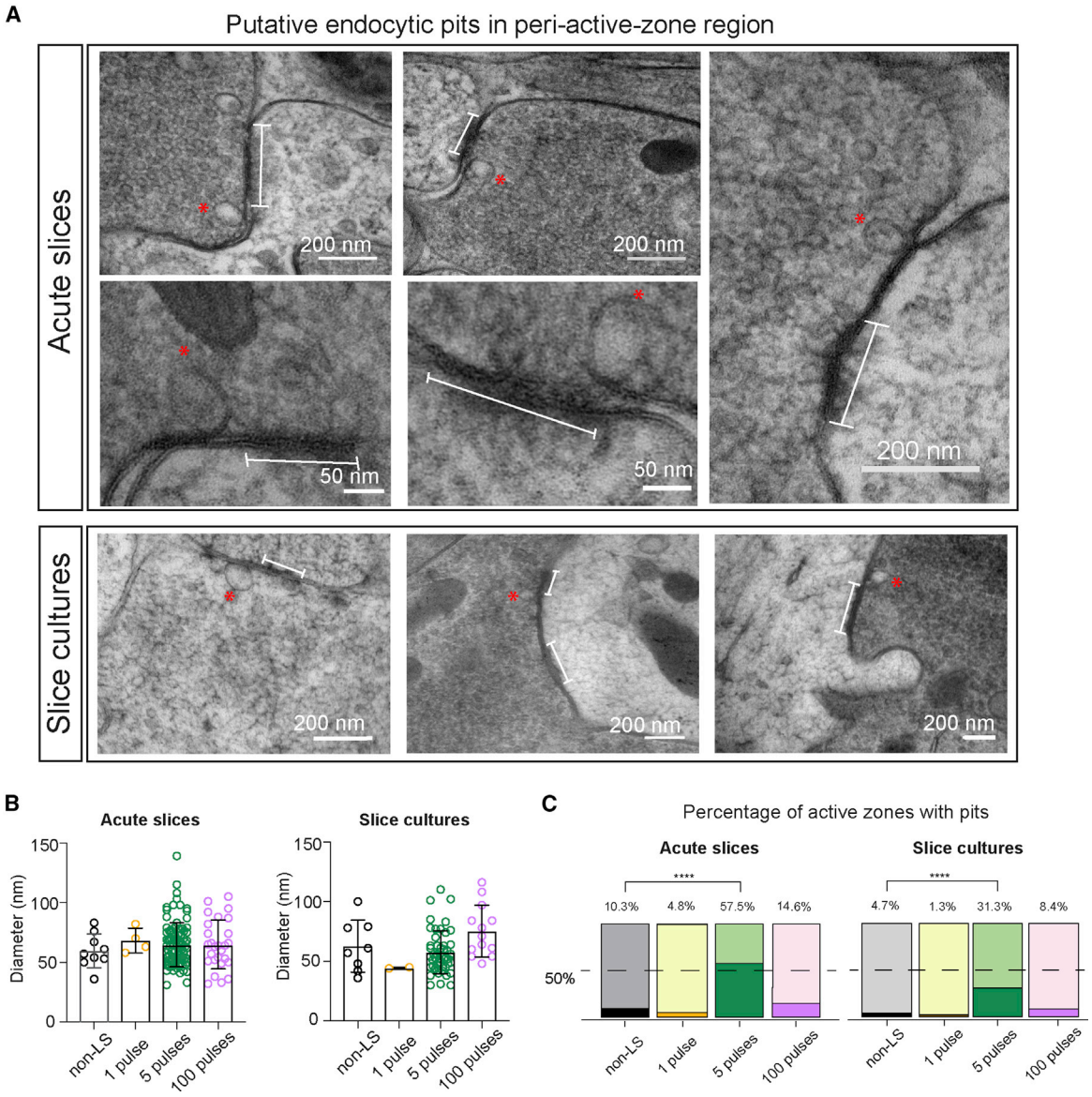

Figure 6. Presence of Putative Endocytic Pits in Peri-active-zone Regions

(A) Example EM micrographs depicting putative endocytic pits (red asterisks) in ASs (top) and SCs (bottom). Note that the AS bottom left corner panel is the same micrograph as shown in Figure S3A, center panel, as a reference to overall tissue morphology quality. Scale bar sizes are indicated in the figure.

(B) Scatterplot displaying the measured diameter of pits under each condition in both ASs and SCs. Bars show mean ± SD. Group statistic comparisons were not significant.

(C) Stacked bars displaying the percentage of active-zones with pits in peri-active-zone regions, per group, in ASs (total active-zones counted: non-LS n = 116 active-zones [AZs], 1 pulse n = 84 AZs, 5 pulses n = 146 AZs, 100 pulses n = 219 AZs) and SCs (total active-zones counted: non-LS, n = 170 AZs; 1 pulse, n = 78 AZs; 5 pulses, n = 160 AZs; 100 pulses, n = 155 AZs). Bars and whiskers denote mean ± SD. For graphical representation of statistics, *p < 0.05, **p < 0.01, ***p < 0.001, and ****p < 0.0001. Only statistically significant differences are shown in the graphs.

functional EM experiments at an identified synapse in an intact cortical network, bridging the gap between structural and functional levels.

Comparison with Previous Approaches

Functional EM ("flash and freeze") has been applied successfully to the *C. elegans* nervous system (Watanabe et al., 2013a) and to dissociated mammalian neurons in culture (Watanabe et al., 2013b). Although the technique is very powerful, it is difficult to apply to intact mammalian preparations, such as organotypic slice cultures or acute brain slices. However, such a development is critically important to use the technique for rigorously identified central synapses and to correlate structural and functional analysis of synaptic transmission (Bischofberger et al., 2006a; Blanton et al., 1989; Edwards et al., 1989; Neher, 2017). We have overcome the limitations of existing techniques

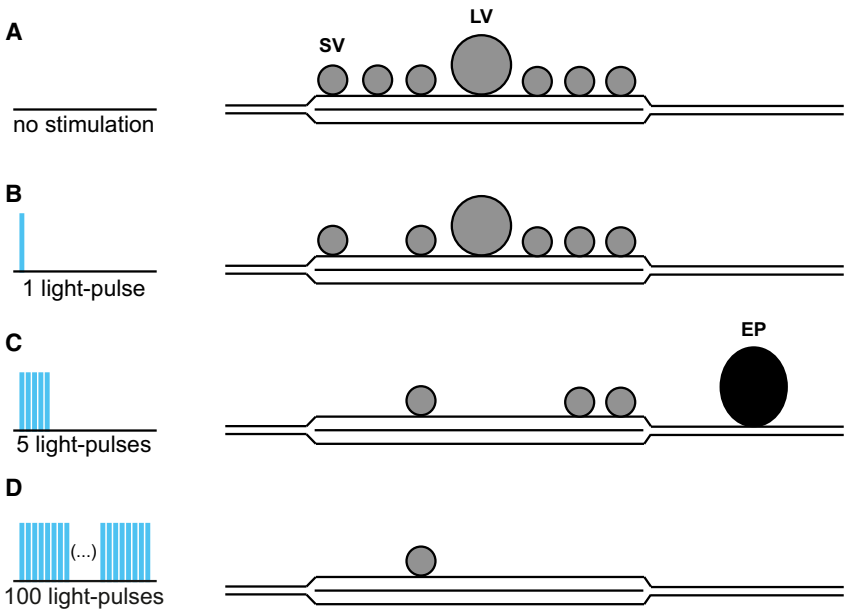

Figure 7. Docked Vesicle Pool Depletion, Activity-Dependent Vesicle Diameter Change, and Fast Endocytosis, as Revealed by Functional EM of Hippocampal Mossy Fiber Terminals

(A–D) From basal conditions (A), we observed a small decrease in docked vesicle numbers after mild stimulation (B and C) but a substantial decrease after a prolonged stimulus train (D). Thus, the docked vesicle pool and RRP overlap at hippocampal mossy fiber terminals. However, docked vesicles were still present at the AZs, indicating that either not all docked vesicles are part of the RRP or that the docked pool is rapidly refilled during the stimulus train. We additionally observed an activity-dependent change in the mean docked vesicle diameter. After a single stimulus (B), the vesicle diameter increased, suggesting that smaller vesicles (SVs) have a higher release probability. After a brief train of stimuli, the mean docked vesicle diameter decreased significantly from the previous group, suggesting that larger vesicles (LVs) were then released. Finally, after mild stimulation (C) with a short train, we observed putative endocytic pits (EPs), providing direct evidence of clathrin-independent endocytosis at the hippocampal mossy fiber synapse.

with a series of technical improvements. First, we reduced the thickness of the acute slices. Second, we introduced a recovery period at near-physiological temperature after slicing, a procedure well established to increase slice quality in electrophysiology experiments (Bischofberger et al., 2006a). Third, we redesigned the specimen sandwich to precisely match the slice thickness and lateral dimensions of the slice without further trimming to maintain the entire target network intact. Fourth, we optimized both concentration and timing of cryoprotection, adding PVP or BSA immediately before stimulation and freezing. We stimulated slices and cultures at physiological temperatures and kept both near physiological temperature for at least 10 min prior to freezing. Finally, we introduced an accelerated freeze substitution protocol. These improvements led to an optimally preserved ultrastructure in acute slices, comparable with the ultrastructure of high-pressure-frozen organotypic slice culture, the previous gold standard for HPF experiments without optogenetic stimulation (Imig et al., 2014; Studer et al., 2014; Zhao et al., 2012a, 2012b).

Potential Limitations

Although the new technique is very powerful, one needs to be aware of unavoidable limitations. First, optogenetics is used to stimulate presynaptic neurons. Although the optogenetically evoked release is clearly AP dependent (Figure 1K), we cannot fully discard the possibility that Ca^{2+} influx through channelrhodopsin may alter release probability, short-term dynamics, or the mode of release (Zhang et al., 2009). Furthermore, the kinetics of the channelrhodopsin set limits to the maximal stimulation frequency. This may be critical in synaptic plasticity experiments where high-frequency stimulation must be used for induction. Second, cryoprotection is an integral component of the technique. Although PVP does not affect transmitter release in electrophysiological experiments (Figure S2D), we cannot exclude that it affects unmeasured functional parameters or structural properties of the synapse. Third, slices are maintained in CO_2 and O_2-equilibrated solution prior to freezing for optimal slice preservation. Because the sandwich mounting is not absolutely gas tight, changes in CO_2 and O_2 partial pressure may negatively affect tissue quality as the time interval between stimulation and freezing is extended.

Insights into Mechanisms of Mossy Fiber Synaptic Transmission

Our results shed new light on the relationship between structure and function of the hippocampal mossy fiber synapse, a key synapse in the trisynaptic circuit of the hippocampus (Andersen et al., 1971; Bischofberger et al., 2006b; Rolls and Treves, 1994; Figure 7). First, our EM analysis shows that the docked vesicle pool at active-zones at hippocampal mossy fiber synapses is substantially reduced by 71.5% after strong stimulation. The most likely explanation is that vesicles are depleted because they undergo full fusion. Although we formally cannot rule out undocking of vesicles, we consider this unlikely because of the slow time course of this process (Murthy and Stevens, 1999). Thus, we conclude that the RRP and docked vesicle pool are highly overlapping (Schikorski and Stevens, 2001; Imig et al., 2014). However, the overlap is not complete. This may suggest that only a subset of docked vesicles is releasable (Ariel and Ryan, 2010) or may be explained by rapid refilling of the docked pool (Wang et al., 2016).

Second, our results confirm that the vesicle diameter at mossy fiber synapses is variable and skewed toward larger diameters, extending previous work on this synapse (Henze et al., 2002; Rollenhagen et al., 2007). Additionally, we found that stimulation reduces the mean diameter of docked vesicles. The most parsimonious explanation is that, during repetitive stimulation, the

smaller vesicles are released first, implying that they have a higher release probability. Consistent with this interpretation, the vesicle fusion rate increases with membrane curvature (Martens et al., 2007; Lin et al., 2012), presumably because curvature stress of the vesicular membrane provides additional energy for bilayer fusion.

Finally, our experiments reveal that moderate repetitive stimulation results in formation of endocytic pits, possibly by a clathrin-independent mechanism. Thus, we provide direct ultrastructural evidence of clathrin-independent endocytosis at the hippocampal mossy fiber synapse, as suggested previously on the basis of capacitance measurements (Hallermann et al., 2003; Delvendahl et al., 2016). However, we did not observe endocytic pits after prolonged stimulation, consistent with previous studies on ultrafast endocytosis (Watanabe et al., 2013a, 2013b). This suggests that endocytosis may be switched to an alternative mode while the initial endocytic pits are cleaved off (Renden and von Gersdorff, 2007; Chanaday and Kavalali, 2018). A potential caveat of our analysis is that we focused on the active-zone and peri-active-zone regions. Endocytic structures may also form at remote sites; for example, near *puncta adherentia* (Watanabe et al., 2013a). Moreover, we examined endocytosis only after 5 and 100 stimuli. Thus, formation of further endocytic structures at later stages cannot be excluded. Future studies with full terminal analysis and at multiple time points will be needed to distinguish between these possibilities. In conclusion, our findings represent a compelling demonstration of the power of this technique, enabling new insights into the basic mechanisms of transmission at identified central synapses.

Future Perspectives

The described method has huge potential for further development. For example, the technique may be combined with post-embedding immunogold or freeze-fracture replica labeling (Nakamura et al., 2015). Such a combination may not only reveal the static molecular organization of presynaptic proteins, such as Ca^{2+} channels, but could demonstrate dynamic changes in the topography of the active-zone. The technique can be also flexibly combined with chemogenetics. This might allow dissection of the mechanisms of presynaptic homeostatic plasticity (Davis and Müller, 2015) using experiments in which chronic chemogenetic manipulation of activity *in vivo* is followed by acute optogenetic stimulation of synapses *in vitro*. Finally, the method can be easily implemented together with pharmacological manipulation. Thus, functional EM may enable structural analysis of pharmacogenetically and pharmacologically manipulated synapses.

We further demonstrated that the technique can be applied to different brain regions and, thus, to a variety of different synapses in intact networks. By genetically targeting specific cell types across different brain areas and, therefore, their synapses, we can expand our understanding of similarities and differences in activity-dependent changes across central synapses. This, in turn, can provide answers to fundamental questions in neuroscience. For example, the new method may help to answer the controversial question of whether synaptic vesicles undergo exocytosis by full fusion or whether a transmitter is released by transient fusion pores (Aravanis et al., 2003; Lisman et al., 2007), as described for dense-core vesicles (Chiang et al., 2014). Furthermore, as a question raised from our data, this approach could address depletion and refilling characteristics of the RRP at mossy fiber boutons and other central synapses. Finally, it may shed light on the mechanisms of short-term plasticity, in which the phenomenon of strengthening of transmission can result from different underlying mechanisms, depending on the synapse; e.g., hippocampal mossy fiber boutons versus calyx of Held (Langdon et al., 1995; Alle et al., 2001; Habets and Borst, 2005).

Because the new method is applicable to both acute slices and organotypic slice cultures, it will enable characterization of the synaptic properties of mouse mutants with lethal phenotypes, which only can be studied in slice culture but not in acute slices (Kerr et al., 2008). The profound similarities as well as the subtle differences between acute slices and organotypic slice culture, quantified in the present paper, will provide a reference framework for interpretation of these results. In a complementary manner, the new technique may be useful to study structural changes induced by disease states, such as epilepsy, which only can be examined in slices but not in culture (Accardi et al., 2018; Wickham et al., 2018). Thus, functional EM techniques applied to intact preparations may help us reveal the structural and functional mechanisms of transmission in intact, genetically perturbed, and disease-affected synapses.

STAR★METHODS

Detailed methods are provided in the online version of this paper and include the following:

- KEY RESOURCES TABLE
- LEAD CONTACT AND MATERIALS AVAILABILITY
- EXPERIMENTAL MODEL AND SUBJECT DETAILS
  - Animals
  - Tamoxifen application
- METHOD DETAILS
  - Tissue preparation
  - Immunofluorescence for confocal microscopy
  - Electrophysiological recordings and light stimulation
  - Pharmacological experiments
  - Preembedding and immunolabeling for electron microscopy
  - High-pressure freezing with light stimulation
  - Freeze-substitution and ultramicrotomy
  - TEM imaging and active-zone profile analysis
- QUANTIFICATION AND STATISTICAL ANALYSIS
- DATA AND CODE AVAILABILITY

SUPPLEMENTAL INFORMATION

Supplemental Information can be found online at https://doi.org/10.1016/j.neuron.2019.12.022.

ACKNOWLEDGMENTS

This project has received funding from the European Research Council (ERC) and European Commission (EC), under the European Union's Horizon 2020 research and innovation programme (ERC grant agreement No.

692692 and Marie Sklodowska-Curie 708497) and from Fonds zur Förderung der Wissenschaftlichen Forschung (Z 312-B27 Wittgenstein award and DK W 1205-B09). We thank Johann Danzl and Ryuichi Shigemoto for critically reading the manuscript; Walter Kaufmann, Daniel Gütl, and Vanessa Zheden for extensive EM training, advice, and experimental assistance; Benjamin Suter for substantial help with light stimulation, ImageJ plugins for analysis, and manuscript editing; Florian Marr and Christina Altmutter for technical support; Eleftheria Kralli-Beller for manuscript editing; Julia König and Paul Wurzinger (Leica Microsystems) for helpful technical discussions; and Taija Makinen for providing the Prox1-CreER^{T2} mouse line.

AUTHOR CONTRIBUTIONS

C.B.-M. (acute slices) and O.K. (organotypic slice culture) performed all experiments and data analysis. C.B.-M., O.K., and P.J. conceived the study and designed experiments. C.B.-M. and P.J. wrote the manuscript. All authors jointly revised the paper.

DECLARATION OF INTERESTS

The authors declare no competing interests.

Received: August 12, 2019
Revised: November 20, 2019
Accepted: December 13, 2019
Published: January 9, 2020

REFERENCES

Accardi, M.V., Huang, H., and Authier, S. (2018). Seizure liability assessments using the hippocampal tissue slice: Comparison of non-clinical species. J. Pharmacol. Toxicol. Methods *93*, 59–68.

Acsády, L., Kamondi, A., Sík, A., Freund, T., and Buzsáki, G. (1998). GABAergic cells are the major postsynaptic targets of mossy fibers in the rat hippocampus. J. Neurosci. *18*, 3386–3403.

Alabi, A.A., and Tsien, R.W. (2012). Synaptic vesicle pools and dynamics. Cold Spring Harb. Perspect. Biol. *4*, a013680.

Alle, H., Jonas, P., and Geiger, J.R.P. (2001). PTP and LTP at a hippocampal mossy fiber-interneuron synapse. Proc. Natl. Acad. Sci. USA *98*, 14708–14713.

Amaral, D.G., and Dent, J.A. (1981). Development of the mossy fibers of the dentate gyrus: I. A light and electron microscopic study of the mossy fibers and their expansions. J. Comp. Neurol. *195*, 51–86.

Andersen, P., Bliss, T.V.P., and Skrede, K.K. (1971). Lamellar organization of hippocampal pathways. Exp. Brain Res. *13*, 222–238.

Aravanis, A.M., Pyle, J.L., and Tsien, R.W. (2003). Single synaptic vesicles fusing transiently and successively without loss of identity. Nature *423*, 643–647.

Ariel, P., and Ryan, T.A. (2010). Optical mapping of release properties in synapses. Front. Neural Circuits *4*, 18.

Bazigou, E., Lyons, O.T., Smith, A., Venn, G.E., Cope, C., Brown, N.A., and Makinen, T. (2011). Genes regulating lymphangiogenesis control venous valve formation and maintenance in mice. J. Clin. Invest. *121*, 2984–2992.

Bischofberger, J., Engel, D., Frotscher, M., and Jonas, P. (2006b). Timing and efficacy of transmitter release at mossy fiber synapses in the hippocampal network. Pflügers Arch. *453*, 361–372.

Bischofberger, J., Engel, D., Li, L., Geiger, J.R.P., and Jonas, P. (2006a). Patch-clamp recording from mossy fiber terminals in hippocampal slices. Nat. Protoc. *1*, 2075–2081.

Blanton, M.G., Lo Turco, J.J., and Kriegstein, A.R. (1989). Whole cell recording from neurons in slices of reptilian and mammalian cerebral cortex. J. Neurosci. Methods *30*, 203–210.

Chanaday, N.L., and Kavalali, E.T. (2018). Optical detection of three modes of endocytosis at hippocampal synapses. eLife *7*, e36097.

Chiang, H.C., Shin, W., Zhao, W.D., Hamid, E., Sheng, J., Baydyuk, M., Wen, P.J., Jin, A., Momboisse, F., and Wu, L.G. (2014). Post-fusion structural changes and their roles in exocytosis and endocytosis of dense-core vesicles. Nat. Commun. *5*, 3356.

Chicurel, M.E., and Harris, K.M. (1992). Three-dimensional analysis of the structure and composition of CA3 branched dendritic spines and their synaptic relationships with mossy fiber boutons in the rat hippocampus. J. Comp. Neurol. *325*, 169–182.

Claiborne, B.J., Amaral, D.G., and Cowan, W.M. (1986). A light and electron microscopic analysis of the mossy fibers of the rat dentate gyrus. J. Comp. Neurol. *246*, 435–458.

Davis, G.W., and Müller, M. (2015). Homeostatic control of presynaptic neurotransmitter release. Annu. Rev. Physiol. *77*, 251–270.

Delvendahl, I., Vyleta, N.P., von Gersdorff, H., and Hallermann, S. (2016). Fast, temperature-sensitive and clathrin-independent endocytosis at central synapses. Neuron *90*, 492–498.

Edwards, F.A., Konnerth, A., Sakmann, B., and Takahashi, T. (1989). A thin slice preparation for patch clamp recordings from neurones of the mammalian central nervous system. Pflügers Arch. *414*, 600–612.

Efron, B., and Tibshirani, R.J. (1998). An introduction to the bootstrap (London: Chapman & Hall/CRC).

Goldammer, H., Hollergschwandtner, E., Elisabeth, N.H., Frade, P.R., and Reipert, S. (2016). Automatized freeze substitution of algae accelerated by a novel agitation module. Protist *167*, 369–376.

Guzman, S.J., Schlögl, A., and Schmidt-Hieber, C. (2014). Stimfit: quantifying electrophysiological data with Python. Front. Neuroinform. *8*, 16.

Habets, R.L., and Borst, J.G.G. (2005). Post-tetanic potentiation in the rat calyx of Held synapse. J. Physiol. *564*, 173–187.

Hallermann, S., Pawlu, C., Jonas, P., and Heckmann, M. (2003). A large pool of releasable vesicles in a cortical glutamatergic synapse. Proc. Natl. Acad. Sci. USA *100*, 8975–8980.

Harris, K.M., and Weinberg, R.J. (2012). Ultrastructure of synapses in the mammalian brain. Cold Spring Harb. Perspect. Biol. *4*, a005587.

Henze, D.A., McMahon, D.B., Harris, K.M., and Barrionuevo, G. (2002). Giant miniature EPSCs at the hippocampal mossy fiber to CA3 pyramidal cell synapse are monoquantal. J. Neurophysiol. *87*, 15–29.

Heuser, J.E., Reese, T.S., Dennis, M.J., Jan, Y., Jan, L., and Evans, L. (1979). Synaptic vesicle exocytosis captured by quick freezing and correlated with quantal transmitter release. J. Cell Biol. *81*, 275–300.

Imig, C., Min, S.W., Krinner, S., Arancillo, M., Rosenmund, C., Südhof, T.C., Rhee, J., Brose, N., and Cooper, B.H. (2014). The morphological and molecular nature of synaptic vesicle priming at presynaptic active zones. Neuron *84*, 416–431.

Kerr, A.M., Reisinger, E., and Jonas, P. (2008). Differential dependence of phasic transmitter release on synaptotagmin 1 at GABAergic and glutamatergic hippocampal synapses. Proc. Natl. Acad. Sci. USA *105*, 15581–15586.

Korogod, N., Petersen, C.C., and Knott, G.W. (2015). Ultrastructural analysis of adult mouse neocortex comparing aldehyde perfusion with cryo fixation. eLife *4*, e05793.

Langdon, R.B., Johnson, J.W., and Barrionuevo, G. (1995). Posttetanic potentiation and presynaptically induced long-term potentiation at the mossy fiber synapse in rat hippocampus. J. Neurobiol. *26*, 370–385.

Lavado, A., Lagutin, O.V., Chow, L.M., Baker, S.J., and Oliver, G. (2010). Prox1 is required for granule cell maturation and intermediate progenitor maintenance during brain neurogenesis. PLoS Biol. *8*, e1000460.

Lin, C.M., Li, C.S., Sheng, Y.J., Wu, D.T., and Tsao, H.K. (2012). Size-dependent properties of small unilamellar vesicles formed by model lipids. Langmuir *28*, 689–700.

Lisman, J.E., Raghavachari, S., and Tsien, R.W. (2007). The sequence of events that underlie quantal transmission at central glutamatergic synapses. Nat. Rev. Neurosci. *8*, 597–609.

Martens, S., Kozlov, M.M., and McMahon, H.T. (2007). How synaptotagmin promotes membrane fusion. Science *316*, 1205–1208.

Ming, G.L., and Song, H. (2011). Adult neurogenesis in the mammalian brain: significant answers and significant questions. Neuron *70*, 687–702.

Miyoshi, G., Young, A., Petros, T., Karayannis, T., McKenzie Chang, M., Lavado, A., Iwano, T., Nakajima, M., Taniguchi, H., Huang, Z.J., et al. (2015). Prox1 regulates the subtype-specific development of caudal ganglionic eminence-derived GABAergic cortical interneurons. J. Neurosci. *35*, 12869–12889.

Möbius, W., Nave, K.A., and Werner, H.B. (2016). Electron microscopy of myelin: Structure preservation by high-pressure freezing. Brain Res. *1641*, 92–100.

Murthy, V.N., and Stevens, C.F. (1999). Reversal of synaptic vesicle docking at central synapses. Nat. Neurosci. *2*, 503–507.

Nakamura, Y., Harada, H., Kamasawa, N., Matsui, K., Rothman, J.S., Shigemoto, R., Silver, R.A., DiGregorio, D.A., and Takahashi, T. (2015). Nanoscale distribution of presynaptic Ca^{2+} channels and its impact on vesicular release during development. Neuron *85*, 145–158.

Neher, E. (2017). Some subtle lessons from the calyx of Held synapse. Biophys. J. *112*, 215–223.

Palay, S.L. (1956). Synapses in the central nervous system. J. Biophys. Biochem. Cytol. *2*, 193–202.

Renden, R., and von Gersdorff, H. (2007). Synaptic vesicle endocytosis at a CNS nerve terminal: faster kinetics at physiological temperatures and increased endocytotic capacity during maturation. J. Neurophysiol. *98*, 3349–3359.

Rizzoli, S.O., and Betz, W.J. (2005). Synaptic vesicle pools. Nat. Rev. Neurosci. *6*, 57–69.

Rollenhagen, A., Sätzler, K., Rodríguez, E.P., Jonas, P., Frotscher, M., and Lübke, J.H.R. (2007). Structural determinants of transmission at large hippocampal mossy fiber synapses. J. Neurosci. *27*, 10434–10444.

Rolls, E.T., and Treves, A. (1994). Neural networks in the brain involved in memory and recall. Prog. Brain Res. *102*, 335–341.

Rosenmund, C., and Stevens, C.F. (1996). Definition of the readily releasable pool of vesicles at hippocampal synapses. Neuron *16*, 1197–1207.

Salin, P.A., Scanziani, M., Malenka, R.C., and Nicoll, R.A. (1996). Distinct short-term plasticity at two excitatory synapses in the hippocampus. Proc. Natl. Acad. Sci. USA *93*, 13304–13309.

Schikorski, T., and Stevens, C.F. (1997). Quantitative ultrastructural analysis of hippocampal excitatory synapses. J. Neurosci. *17*, 5858–5867.

Schikorski, T., and Stevens, C.F. (2001). Morphological correlates of functionally defined synaptic vesicle populations. Nat. Neurosci. *4*, 391–395.

Stoppini, L., Buchs, P.A., and Muller, D. (1991). A simple method for organotypic cultures of nervous tissue. J. Neurosci. Methods *37*, 173–182.

Studer, D., Zhao, S., Chai, X., Jonas, P., Graber, W., Nestel, S., and Frotscher, M. (2014). Capture of activity-induced ultrastructural changes at synapses by high-pressure freezing of brain tissue. Nat. Protoc. *9*, 1480–1495.

Vyleta, N.P., Borges-Merjane, C., and Jonas, P. (2016). Plasticity-dependent, full detonation at hippocampal mossy fiber-CA3 pyramidal neuron synapses. eLife *5*, e17977.

Wang, S.S.H., Held, R.G., Wong, M.Y., Liu, C., Karakhanyan, A., and Kaeser, P.S. (2016). Fusion competent synaptic vesicles persist upon active zone disruption and loss of vesicle docking. Neuron *91*, 777–791.

Watanabe, S., Liu, Q., Davis, M.W., Hollopeter, G., Thomas, N., Jorgensen, N.B., and Jorgensen, E.M. (2013a). Ultrafast endocytosis at Caenorhabditis elegans neuromuscular junctions. eLife *2*, e00723.

Watanabe, S., Rost, B.R., Camacho-Pérez, M., Davis, M.W., Söhl-Kielczynski, B., Rosenmund, C., and Jorgensen, E.M. (2013b). Ultrafast endocytosis at mouse hippocampal synapses. Nature *504*, 242–247.

Wickham, J., Brödjegård, N.G., Vighagen, R., Pinborg, L.H., Bengzon, J., Woldbye, D.P.D., Kokaia, M., and Andersson, M. (2018). Prolonged life of human acute hippocampal slices from temporal lobe epilepsy surgery. Sci. Rep. *8*, 4158.

Zhang, Q., Li, Y., and Tsien, R.W. (2009). The dynamic control of kiss-and-run and vesicular reuse probed with single nanoparticles. Science *323*, 1448–1453.

Zhao, S., Studer, D., Chai, X., Graber, W., Brose, N., Nestel, S., Young, C., Rodriguez, E.P., Saetzler, K., and Frotscher, M. (2012a). Structural plasticity of hippocampal mossy fiber synapses as revealed by high-pressure freezing. J. Comp. Neurol. *520*, 2340–2351.

Zhao, S., Studer, D., Graber, W., Nestel, S., and Frotscher, M. (2012b). Fine structure of hippocampal mossy fiber synapses following rapid high-pressure freezing. Epilepsia *53*, 4–8.

STAR★METHODS

KEY RESOURCES TABLE

REAGENT or RESOURCE	SOURCE	IDENTIFIER
Antibodies		
Rabbit Polyclonal anti-NeuN	Invitrogen (Thermo fisher)	RRID: AB_2554049
Goat anti-rabbit Alexa Fluor 647	Molecular Probes (Thermo fisher)	RRID: AB_141663
Rabbit Polyclonal anti-GFP	Abcam	RRID: AB_305564
Goat anti-rabbit Biotinylated IgG	Vector Laboratories	RRID: AB_2313606
Chemicals, Peptides, and Recombinant Proteins		
Tamoxifen	Sigma-Aldrich	Cat # T5648-1G
4-hydroxy-tamoxifen	Sigma-Aldrich	Cat # H7904-5mg
NaCl	VWR (Merck)	Cat # 1.06404.1000
Sucrose	Sigma-Aldrich	Cat # 16104
$NaHCO_3$	VWR (Merck)	Cat # 1.06329.1000
D-glucose	VWR (Merck)	Cat # 1.08342.1000
KCl	VWR (Merck)	Cat # 26764.232
NaH_2PO_4	VWR (Merck)	Cat # 1.06346.0500
$CaCl_2$	VWR (Merck)	Cat # 1.02382.0250
$MgCl_2$	Honeywell	Cat # M9272-1KG
HEPES	Sigma-Aldrich	Cat # M3375-100G
EGTA	Sigma-Aldrich	Cat # EO396-100G
Na_2ATP	Sigma-Aldrich	Cat # A3377-100G
Hank's Balanced Salt Solution (HBSS)	GIBCO	Cat # 24020091
20% D-Glucose	Braun	Cat # 2356746
Minimum Essential Medium	GIBCO	Cat # 11095-080
Basal medium eagle	Invitrogen	Cat # 41010026
Horse serum	GIBCO	Cat # 26050070
Glutamax	GIBCO	Cat # 35050-061
NaH_2PO_4 $2H_2O$ (for PBS)	VWR (Merck)	Cat # 1.06580.0500
Paraformaldehyde 20%	TAAB	Cat # FO 17/1
Normal goat serum	Dianova	Cat # 005-000-121
Trition X – 100	Sigma-Aldrich	Cat # X100-100ml
DAPI, dilactate	Sigma-Aldrich	Cat # D9564-10mg
Prolong Gold antifade	Invitrogen	Cat # P36934
Tetrodotoxin citrate	Alomone Labs	Cat # T-550
polyvinylpyrrolidone (PVP)	Sigma-Aldrich	Cat # PVP10-100G
Bovine serum albumin (BSA)	Sigma-Aldrich	Cat # A9647-100G
Glutaraldehyde 25%	Carl Roth	Cat # 4157.1
Sodium Azide	Sigma-Aldrich	Cat # S8032-25G
Tris (for TBS)	Sigma-Aldrich	Cat # 25,285-9
Streptavidin biotin complex (ABC Kit)	Vector laboratories	Cat # PK-6100
3,3′ DAB (Diaminobenzidin)	Sigma-Aldrich	Cat # D5637-5G
Osmium tetroxide	Science services (EMS)	Cat # 19130
Durcupan ACM Resin Single component A	Sigma-Aldrich	Cat # 44611-100ml
Durcupan ACM Resin Single component B	Sigma-Aldrich	Cat # 44612-100ml
Durcupan ACM Resin Single component C	Sigma-Aldrich	Cat # 44613-100ml
Durcupan ACM Resin Single component D	Sigma-Aldrich	Cat # 44614-100ml

(*Continued on next page*)

Continued		
REAGENT or RESOURCE	SOURCE	IDENTIFIER
Uranyl acetate $2H_2O$	Serva	Cat # 77870.02
Lead (II) Nitrate	Sigma-Aldrich	Cat # 228621-100G
Acetone, HPLC grade	ChemLab	Cat # CL00.0172.2500
Experimental Models: Organisms/Strains		
Prox1-CreER^{T2} mouse line	Bazigou et al., 2011	PMID: 21765212
C57BL6/J wild-type mice	Charles River Germany (from The Jackson Laboratory)	RRID: IMSR_JAX:000664
Tg(Prox1-Cre)SJ32Gsat/Mmucd mouse line	Mutant Mouse Resource & Research Centers	RRID: MMRRC_036644-UCD
B6;129S6-Gt(ROSA)26Sor$^{tm9(CAG-tdTomato)Hze}$/J mouse line	The Jackson Laboratory	RRID: IMSR_JAX:007905
B6;129S-Gt(ROSA)26Sor$^{tm32(CAG-COPA*H134R/EYFP)Hze}$/J mouse line	The Jackson Laboratory	RRID: IMSR_JAX:012569
Software and Algorithms		
Multiclamp (version 1.3.0.05)	Axon Instruments/Molecular Devices	https://www.moleculardevices.com/
Igor Pro (version 6.3.4.1)	WaveMetrics	https://www.wavemetrics.com/
Radius Software	EMSIS	https://www.emsis.eu/products/software/radius/
Stimfit (version 0.14.13)	Guzman et al., 2014	PMID: 24600389
AxoGraph (version 1.7.2)	AxoGraph	https://axograph.com/
Fiji (ImageJ version 2.0.0-rc-69/1.52n)	NIH, Open source	https://fiji.sc/
Graphpad Prism (version 8)	Graphpad	https://www.graphpad.com/
Adobe Illustrator (version 23.0.4)	Adobe	https://www.adobe.com/products/illustrator.html
Imaris	Oxford Instruments	https://imaris.oxinst.com/
Other		
Membrane insert (sterilized culture plate insert)	Millicell-CM, Millipore	PICMORG50

LEAD CONTACT AND MATERIALS AVAILABILITY

Further information and requests for resources and reagents should be directed to and will be fulfilled by the Lead Contact, Peter Jonas (peter.jonas@ist.ac.at). This study did not generate new unique reagents.

EXPERIMENTAL MODEL AND SUBJECT DETAILS

Animals

Experiments were performed in acute slices or organotypic slice cultures from male and female mice. For acute slice experiments, slices were prepared from 25–40-day-old mice (P25–40). This age range represents fully developed mossy fiber terminals, as maturation happens at P21 (Chicurel and Harris, 1992; Claiborne et al., 1986; Amaral and Dent, 1981). For organotypic slice culture experiments, tissue was extracted from 5–8-day-old mice (P5–8). Cre-driver lines used in this study were a Prox1-CreER^{T2} line (Bazigou et al., 2011; PMID: 21765212) and a Tg(Prox1-Cre)SJ32Gsat/Mmucd line (Mutant Mouse Resource & Research Centers; RRID:MMRRC_036644-UCD) (for Figure S1). Reporter lines were a B6;129S6-Gt(ROSA)26Sor$^{tm9(CAG-tdTomato)Hze}$/J line (The Jackson Laboratory; line #007905; RRID: IMSR_JAX:007905) and a B6;129S-Gt(ROSA)26Sor$^{tm32(CAG-COPA*H134R/EYFP)Hze}$/J line (The Jackson Laboratory; line #012569; RRID:IMSR_JAX:012569), as well as C57BL6/J wild-type animals (Charles River Germany, from The Jackson Laboratory; line #000664; RRID:IMSR_JAX:000664). Transgenic mice were genotyped by PCR, with DNA extracted from toe or ear clippings.

Tamoxifen application

For acute slice experiments, tamoxifen (Sigma-Aldrich) injections were made from a stock solution of 20 mg ml^{-1} in corn oil (Sigma-Aldrich). For maximum expression of channelrhodopsin in GCs, each mouse received two intraperitoneal (IP) injections of tamoxifen at 100 mg kg^{-1} of mouse body weight, given 2–3 days apart. Mice were used for experiments after a minimum of 7–10 days after

injections. For organotypic slice culture experiments, 5 μM of 4-hydroxy-tamoxifen (Sigma-Aldrich) was added to culture medium for 24 hours on the 7th day *in vitro* (DIV). Cultures were then used for experiments 2–3 weeks (21–28 DIV) after tamoxifen application. Animals were bred in a colony maintained in the preclinical animal facility at IST Austria. All procedures strictly complied with IST Austria, Austrian, and European ethical regulations for animal experiments, and were approved by the Bundesministerium für Wissenschaft, Forschung und Wirtschaft of Austria (BMWFW-66.018/0010-WF/V/3b/2015 and BMWFW-66.018/0008-V/3b/2018).

METHOD DETAILS

Tissue preparation

Acute slices were prepared as previously described for optimal preservation of the hippocampal mossy fiber tract (Bischofberger et al., 2006a). Mice were lightly anaesthetized with isoflurane and rapidly decapitated. The brain was dissected from the skull and blocked with a "magic-cut" under ice-cold high-sucrose solution containing: 87 mM NaCl, 75 mM sucrose, 25 mM $NaHCO_3$, 10 mM D-glucose, 2.5 mM KCl, 1.25 mM NaH_2PO_4, 0.5 mM $CaCl_2$, and 7 mM $MgCl_2$, equilibrated with 5% CO_2 and 95% O_2. Transverse hippocampal slices were sectioned at 200–300 μm thickness for electrophysiology experiments and at 150–200 μm for high-pressure freezing (HPF), using a vibratome (VT1200S, Leica Microsystems) in ice-cold high-sucrose solution. Slices were transferred to a maintenance chamber, and recovered at 35°C for 30–45 min. For HPF, slices from left and right hemisphere were stored in different chambers (see STAR Methods section for High-Pressure Freezing with Light Stimulation). After recovery, slices were kept at room temperature (~23°C) until recording, for up to 4–5 hours. For HPF, after recovery and until freezing, slices were transferred to a second set of maintenance chambers filled with ACSF solution, identical to solution used for electrophysiology recordings, containing: 125 mM NaCl, 25 mM $NaHCO_3$, 25 mM D-glucose, 2.5 mM KCl, 1.25 mM NaH_2PO_4, 2 mM $CaCl_2$, and 1 mM $MgCl_2$, equilibrated with 5% CO_2 and 95% O_2. Finally, 5–10 min prior to freezing, slices were transferred into a chamber filled ACSF at 37°C, as all freezing experiments were performed from physiological temperature (37°C). Sagittal cerebellum slices and coronal brainstem slices (200 μm thickness) were cut with identical procedures.

Hippocampal organotypic slice cultures were prepared from both hemispheres using the Stoppini-type method (Stoppini et al., 1991; Kerr et al., 2008). The entire hippocampus with entorhinal cortex was dissected and cut, perpendicularly to the longitudinal axes, using a McIllwain tissue chopper. Hippocampus extraction and cutting were performed in a medium containing Hanks' Balanced Salt Solution (HBSS, GIBCO) and 20% D-glucose (Braun). Slices were placed on microporous membrane inserts (Millicell, Millipore) floating on culture media containing 50% minimum essential medium, 25% basal medium Eagle, 25% heat-inactivated horse serum, 2 mM glutamax (all from GIBCO), and 0.62% D-glucose (Braun), pH 7.2. Slice cultures were kept at 37°C and 5% CO_2, until used for HPF or electrophysiology experiments. Note that there are limitations to the slice culture system, including the possibility of enhanced connectivity.

Immunofluorescence for confocal microscopy

For immunohistochemistry (Figure S1A and S1B), mice were anaesthetized with isoflurane and transcardially perfused with warm (~37°C) 0.1 M phosphate buffer (PB) solution, pH 7.35, followed by ice-cold 4% paraformaldehyde (PFA) in 0.1 M PB. Brains were dissected, incubated overnight in 4% PFA and rinsed with 0.1 M PB prior to sectioning. Hippocampal horizontal sections (50 μm thickness) were cut in 0.1 M PB using a vibratome (Leica VT1200S). Organotypic slice cultures were fixed using 4% PFA in 0.1 M PB at 4°C for 30 min, after 14 DIV. After sectioning or, for cultures, directly after fixing, the tissue was washed in 0.1 M PB and subsequently incubated for 1 hour in blocking solution (10% normal goat serum (NGS) in PB). Next, tissue was incubated for 72 hours with primary antibody (0.1 M PB with 0.4% Triton, 5% NGS and 1:500 rabbit anti-NeuN; Thermo Fisher Scientific Cat# PA5-37407, RRID: AB_2554049) at 4°C, followed by washes with 0.1 M PB. Subsequently, tissue was incubated for 24 hours with secondary antibody (0.1 M PB with 0.3% Triton, 5% NGS and 1:1000 goat anti rabbit Alexa 647; Molecular Probes Cat# A-21244, RRID: AB_141663). Samples were then washed and incubated in DAPI (0.00003 mg ml^{-1}) for 10 min. Finally, sections were mounted in Prolong Gold antifade embedding medium (Invitrogen). Fluorescence images were acquired using a confocal microscope (Leica SP5 upright) with sequential scanning of fluorescent signals using an air-objective (10x / numerical aperture 0.3 or 20x / numerical aperture 0.5). Confocal images were analyzed with Fiji open source software. Cell-counting for the tamoxifen dose-response curve was done in Imaris (Oxford Instruments).

Electrophysiological recordings and light stimulation

After tissue preparation, slices and cultures were transferred to a recording chamber and superfused with ACSF. Recordings were performed at near-physiological temperature. For acute slice recordings, slices were visualized with a Zeiss Axioskop 2 FS Plus microscope, equipped with DIC optics and a 60x water immersion Olympus objective. For slice culture experiments, a Zeiss Axio Examiner D1 microscope and a 63x water immersion Zeiss Plan-Apochromat objective was used. For excitation of tdTomato and channelrhodopsin, a high-power LED head (LED4D212; Thorlabs) and 4-channel LED driver (DC4104; Thorlabs) were used in combination with Semrock BrightLine single-band bandpass filters 536/40 nm and 607/70 nm with a 562 nm dichroic mirror for tdTomato excitation, and 458/64 nm and 531/40 nm with a 506 nm dichroic mirror for channelrhodopsin stimulation with 470 nm wavelength. The light path was optimized so that the light intensity at the tissue surface with wide-field stimulation with a 10x objective closely

resembled that of the Leica EM ICE high-pressure freezing machine LED range (intensity at specimen 5.5–8.0 mW mm^{-2}). Timing and intensity of light pulses were repeatedly checked by photodiode measurements.

Patch electrodes were pulled from borosilicate glass capillaries (2 mm outer diameter, 0.5 mm wall thickness; Hilgenberg) with a horizontal puller (P-1000, Sutter Instrument). For whole-cell recordings in acute slices and cultures, pipettes were filled with intracellular solution containing: 148 mM K-gluconate, 2 mM KCl, 2 mM $MgCl_2$, 2 mM Na_2ATP, 10 mM EGTA, and 10 mM HEPES (297–300 mOsm, pH 7.28), with a holding potential of −70 mV, and chloride reversal potential of −82 mV. Signals were recorded with a Multiclamp 700A (acute slices) or an Axopatch 200A amplifier (slice cultures) (Axon Instruments) and digitized with a CED 1401 plus interface (Cambridge Electronic Design). Pulse generation and data acquisition were performed using FPulse version 3.3.3 (U. Fröbe, Freiburg, Germany) and Igor Pro version 6.3.4.1 (WaveMetrics). Data were analyzed with Stimfit version 0.14.13 (Guzman et al., 2014) or Axograph Software version 1.7.2.

Pharmacological experiments

During electrophysiology recordings, tetrodotoxin (TTX) (voltage-gated Na^+ channels, BioTrend or Alomone Labs) and PVP were delivered by bath application at concentrations specified in the results section. For HPF control experiments, samples were incubated with TTX-containing ACSF for ~10 min prior to freezing.

Preembedding and immunolabeling for electron microscopy

For EM preembedding immunolabeling experiments (Figure S1D), animals were perfused as described for confocal light-microscopy, but with ice-cold 4% PFA and 0.05% glutaraldehyde in 0.1 M PB, pH 7.4. Brains were sectioned at 70 μm in 0.1 M PB and sections were stored in 0.025% NaN_3 in PB at 4°C. For cryo-protection, samples were transferred to sucrose solutions of increasing concentration (5%, 10%, and 20% in PB), for 1 hour each and left overnight in 20% sucrose solution at 4°C. Samples were transferred to a 12-well plate. Next, plates were placed directly onto liquid nitrogen (floating) for about 1 min. The plate was removed and samples were thawed rapidly with large volumes of 0.1 M PB. Samples were re-infiltrated with 20% sucrose and freeze-thaw was repeated 2 to 3 times. For immunolabeling, samples were first washed in 50 mM Tris-buffered saline (TBS; 0.9% NaCl, pH 7.4). Next, sections were incubated in 50 mM glycine in TBS for 1 hour, blocked in 10% normal serum and 2% BSA in TBS, and incubated in rabbit polyclonal anti-GFP primary antibody (1:5000, Abcam Cat# ab6556, RRID: AB_305564) for 36 hours at 4°C in TBS with 2% BSA. After wash in TBS, sections were incubated with biotinylated IgG anti-rabbit secondary antibody (1:400, Vector Laboratories Cat# BA-1000, RRID: AB_2313606) in TBS with 2% BSA overnight at 4°C. Next, samples underwent reaction with streptavidin biotin complex (ABC kit, Vector laboratories). Solution A (1/100) and B (1/100) were mixed in TBS with 0.2% BSA and samples were incubated for 3 hours. Samples were then washed in TBS, followed by only tris buffer (TB), at room temperature. Next, samples were incubated in 0.5 mg ml^{-1} DAB in TB for 5 min, with 0.003% hydrogen peroxide in TB, and washed in TB. Subsequently, samples were washed and post-fixed in 1% glutaraldehyde in 0.1 M phosphate buffer (PB) for 20 min. Samples were contrasted by incubation with 1% osmium tetroxide (Science Services) in 0.1 M PB for 45 min followed by incubation in 1% uranyl acetate and 50% ethanol for 30 min in darkness. Next they went through a series of dehydration steps in ethanol and infiltrated in propylene oxide, followed by infiltration with 1:2 and 2:1 Durcupan resin (10 g reagent A, 10 g B, 0.3 g C, and 0.3 g D) and propylene oxide mix, and embedded in pure Durcupan resin overnight.

High-pressure freezing with light stimulation

HPF was performed with a Leica EM ICE high-pressure freezing apparatus (Leica Microsystems) equipped with a blue LED light stimulation module 460 nm wavelength; LED intensity at specimen 5.5–8.0 mW mm^{-2}). The Leica EM ICE specimen assembly table was kept at 40°C at all times during specimen sandwich assembly to keep all materials and samples close to physiological temperature. The freezing chamber was kept at 37°C. After slicing and recovery procedures, hippocampal acute slices were frozen in filler medium containing 15% PVP (Sigma Aldrich) in ACSF, equilibrated with 5% CO_2 and 95% O_2 and kept at 37°C. We tested carrier filler medium with ACSF alone, ACSF with 20% BSA, and ACSF with varying concentrations of PVP from 5 to 20% (Möbius et al., 2016). We noticed that spontaneously opened sapphire sandwiches immediately after freezing had a higher likelihood of leading to damaged acute slice samples. The use of 15% PVP was ideal to both prevent sandwich opening after freezing, but also avoid irreversible tissue adherence to the sapphires. The specimen sandwich was assembled with a 6-mm diameter sapphire system, including transparent half-cylinder cartridges (Leica) for light stimulation, a middle-plate (Leica), two 120 μm sapphire disks, a 150 or 200-μm thick spacer ring, and a 450- or 400-μm thick top ring (Leica or Engineering Office M. Wohlwend, Sennwald, Switzerland) as required (Figure S2). The outer diameter of sapphire disks and rings was 6 mm. The inner diameter of the rings was 5 mm for larger slices and 4 mm for smaller slices. We found that sandwiches assembled with 4 mm inner diameter rings were more stable and the sapphire disks were less likely to break, however infiltration during freeze-substitution took longer. The order of assembly was as follows: the bottom sapphire disk was placed on the middle plate, followed by the spacer ring with a drop of filler medium over the ring to adhere it to the sapphire disk, the sample, and the top sapphire disk. Slices were transferred carefully but quickly to the sapphire disk, using a paintbrush number 4, always covered with solution, keeping the slice as flat as possible. The optical fiber for light stimulation was located on the top of the freezing chamber. Left and right hemispheres were frozen separately, for unequivocal tracking of the light-stimulated side based on hippocampal morphology, until embedding with the light-stimulated side facing down. Organotypic slice cultures were taken out of the incubator and the tissue attached to membrane was cut out with a 4-mm biopsy punch (Ted Pella). The time

from taking the slice cultures out of incubator until freezing was less than 10 min. Cryoprotectant use on cultures was tested at a range of 5%–20% BSA and the optimum concentration resulting in best ultrastructure was obtained with filler medium containing 15% BSA (Sigma-Aldrich) in ACSF at 37°C (Studer et al., 2014). For freezing cultures, "hybrid" sandwiches were used. They consisted of a 6 mm metal carrier (5 mm inner diameter, type A, Leica) at the bottom, and a 6 mm, 120-μm thick sapphire disk, and a 200-μm thick top ring (Wohlwend) on the top. Each culture, with the membrane facing down, was placed in the metal carrier well covered with filler solution and closed with the sapphire disk for subsequent light stimulation. This configuration increased the stability of the sandwich and the control of light-stimulated side orientation, as it was always facing the sapphire disk.

Freeze-substitution and ultramicrotomy

We tested different FS protocols based on other studies that used HPF in fresh (non-fixed) tissue, both organotypic slice cultures and acute slices (Studer et al., 2014), and organotypic slice cultures alone (Imig et al., 2014). As the previously used protocols were several days long, we implemented a shaking device that fits on top of the automated freeze-substitution (AFS) apparatus (Goldammer et al., 2016), to shake the samples throughout the procedure to improve infiltration and shorten the duration. Additionally, we tested protocols with and without tannic acid, with different concentrations of osmium tetroxide, with and without shaking (i.e., different duration), and different temperature steps and various post-staining parameters. The final protocol more closely resembled the one developed by Studer et al. (2014). For the first day of freeze-substitution, the HPF samples were transferred from liquid nitrogen to vials with 0.1% tannic acid in acetone, frozen in liquid nitrogen. Vials were then transferred to either a Leica EM AFS1 or AFS2 kept at −90°C and shaken for 22–24 hours. For acute slice samples frozen with spacer rings with 4 mm inner diameter, samples were shaken longer, for at least 26 hours to ensure that the sandwich opens for proper infiltration. On the second day, samples were washed 3–4 times, while kept inside the FS machines, with acetone chilled to −90°C for 10 min each. Next, the contrasting cocktail with 2% osmium and 0.2% uranyl acetate in acetone, also first chilled to −90°C, was added to each vial and shaken overnight. For acute slices, samples were kept at −90°C for 7–10 hours. For organotypic slice cultures, samples were kept at −90°C for 6 hours. Next, the temperature was raised to −60°C within 2 hours (15°C/hour) and kept at −60°C for 3 hours (3.5 hours for 4-mm diameter spacers); then raised to −30°C in 4 hours (7.5°C/hour), and kept at −30°C for 3 hours (3.5 hours for 4-mm inner diameter spacers); then raised to 0°C in 3 hours (10°C/hour). Samples were kept at 0°C only for ~10 min. Once the substitution protocol was concluded, the vials were transferred to ice for washes with ice-cold acetone, 3 times for 10 min each. They were then transferred to room-temperature glass dishes, always submerged in acetone, to visually check that the slices and cultures were intact, all sandwiches properly opened, and the tissue adequately infiltrated. They were then washed twice with propylene oxide for 10 min each and infiltrated with hard Durcupan resin (11.4 g reagent A, 10 g B, 0.3 g C, and 0.1 g D) at 2:1, 1:1, and 1:2 propylene oxide/Durcupan resin mix for 1 hour each, shaking. They were then left in pure resin overnight and embedded in BEEM capsules. Capsules were polymerized overnight at 100°C. Acute slices were embedded with care to ensure that the light-stimulated side of the slice was facing down. Each slice culture was separated from the carrier and embedded with stimulated tissue (not membrane side) facing down for ultramicrotomy. Cured resin blocks were trimmed with glass knives and 70 nm ultrathin sections were cut with a Leica EM UC7 ultramicrotome with Diatome Histo diamond knives. Sections were picked up on Formvar-coated copper slot grids for transmission electron microscopy (TEM) imaging. Post-staining was done in 2 or 4% uranyl acetate for 10 minutes followed by lead citrate for 2–3 minutes.

TEM imaging and active-zone profile analysis

Parameters used to recognize well-preserved frozen samples and identified synapses were: overall appearance with minimal evidence of extracellular space, smooth and continuous membrane surfaces, double membranes regularly spaced, easily recognizable compact mitochondria with regular and visible cristae, cell bodies and dendrites with abundant microtubules, and nuclei with uniform chromatin (Studer et al., 2014). Hippocampal mossy fiber boutons were identified in the hippocampal CA3b and CA3c subregions. They were found in high density along the mossy fiber tract in *stratum lucidum*, adjacent to *stratum pyramidale*. They were recognized based on previously well-characterized morphological features large size, high density of clear synaptic vesicles, presence of large dense core vesicles, high-density of mitochondria, multiple active-zones apposed to postsynaptic densities in large spines, and nonsynaptic *puncta adhaerentia* apposed to dendritic shafts. We found that near the surface of acute slices, ultrastructure was compromised, presumably by the cutting procedure. This observation was not unexpected, as it is also the case for electrophysiology experiments (Bischofberger et al., 2006a). Near the core of the slice, crystalline ice was occasionally formed during freezing. Thus, we focused our analysis on a region 20–50 μm below the surface of the slice. This range corresponds also to the acute slice depth used for electrophysiology recordings in Figure 1.

Images of ultrathin sections were taken with a transmission electron microscope (Thermo Fisher/FEI Tecnai 10, 80 kV acceleration voltage) with an OSIS Megaview III G3 camera and Radius acquisition software. All electron microscopy images were analyzed with Fiji open source software. Brightness and contrast were adjusted in Fiji, according to inherent contrast of the image, to optimize double membrane visualizations and accurate measurements. Vesicles that were less than 5 nm from the active-zone membrane were considered "docked" (Figure S6). Numbers of docked vesicles per profile were specified per 100 nm of active-zone length for reliable comparison. For direct comparison across groups, raw histogram counts were divided by the total length of active-zone analyzed for each corresponding experimental condition. The resulting histograms display vesicle density (per 100 nm of active-zone) as a function of vesicle diameter. All vesicle counting and imaging analyses were done with the experimenter blind to the condition tested on the sample.

QUANTIFICATION AND STATISTICAL ANALYSIS

Analyses were performed with Prism 8 (GraphPad Software). All data were first tested for normality with D'Agostino-Pearson test. Statistical comparison of all data groups were tested by Kruskal-Wallis non-parametric one-way ANOVA, followed by Dunn's post hoc multiple comparison test. Groups with only two datasets were compared using unpaired or paired t test (electrophysiology data) or two-tailed non-parametric Mann-Whitney U test (morphological data). For graphical representation of statistics, * indicates $p < 0.05$, ** $p < 0.01$, *** $p < 0.001$, and **** $p < 0.0001$. In figures and text, values report, as specifically stated, mean or median, and errors standard deviation.

To determine whether distributions of vesicle diameter were comprised of one or two components, unbinned vesicle diameter data were analyzed by maximum likelihood fitting. Data were fit with a single normal distribution, a sum of two normal distributions, a skewed normal distribution, and a function with a sigmoidal rise, exponential decline, and shift. The model with two normal distributions was compared against all other models, using the log-likelihood ratio. Statistical significance values were obtained by bootstrap analysis (Efron and Tibshirani, 1998). Original data were duplicated 1000 times, shuffled by random permutation, and re-segmented into blocks of original length, resulting in 1000 resampled datasets. These datasets were analyzed by maximum-likelihood fitting, similar to the original data. Finally, the distribution of the log–likelihood ratios was compared against the Akaike information criterion. To provide a rigorous testing of the two-component model, the log likelihood for the best one-component model was used for comparison.

DATA AND CODE AVAILABILITY

Original data and analysis programs will be provided by the corresponding authors (C.B.M. and P.J.) upon reasonable request. Computer code was not generated in this study.